Influence of local cubic anisotropy on the transition towards an equipartition regime in a 3D texture-less random elastic medium

Shahram Khazaie, Régis Cottereau

▶ **To cite this version:**

Shahram Khazaie, Régis Cottereau. Influence of local cubic anisotropy on the transition towards an equipartition regime in a 3D texture-less random elastic medium. Wave Motion, 2020, 96, pp.102574. 10.1016/j.wavemoti.2020.102574 . hal-02566857

HAL Id: hal-02566857
https://hal.science/hal-02566857v1

Submitted on 7 May 2020

HAL is a multi-disciplinary open access archive for the deposit and dissemination of scientific research documents, whether they are published or not. The documents may come from teaching and research institutions in France or abroad, or from public or private research centers.

L'archive ouverte pluridisciplinaire **HAL**, est destinée au dépôt et à la diffusion de documents scientifiques de niveau recherche, publiés ou non, émanant des établissements d'enseignement et de recherche français ou étrangers, des laboratoires publics ou privés.

Influence of local cubic anisotropy on the transition towards an equipartition regime in a 3D texture-less random elastic medium

Shahram Khazaie[a,*], Régis Cottereau[b]

[a] *Université de Nantes, GeM, Institut de Recherche en Génie Civil et Mécanique, Équipe E3M, Saint-Nazaire, France*
[b] *Aix Marseille Univ, CNRS, Centrale Marseille, LMA UMR 7031, Marseille, France*

Abstract

At long lapse times in randomly fluctuating media with macroscopic isotropy (texture-less media), the energy of elastic waves is equipartitioned between compressional (P) and shear (S) waves. This property is independent of the local isotropy or anisotropy of the heterogeneous constitutive tensor and of the type of source. However the local symmetry of the constitutive tensor does influence the rate of convergence to equipartition and this paper discusses the precise influence of local anisotropy on the time required to reach equipartition. More particularly, a randomly-fluctuating medium is considered, whose behavior is statistically isotropic, and locally cubic. After calculating all the differential and total scattering cross-sections in that case, an analytical formula is derived for the rate of convergence to the equipartition regime, function of the second-order statistics of the mechanical parameter fields (bulk and shear moduli and anisotropy parameter). The local anisotropy is shown to influence strongly that transition rate, with a faster transition when the fluctuations of the anisotropy parameter are positively correlated to those of the shear modulus. A numerical model is constructed to illustrate numerically these results. Since the asymptotic regime of equipartition cannot be simulated directly because it would require too large a computational domain, boundaries are introduced and mechanical properties are chosen so as to minimize their influence on equipartition.

Keywords: Random medium, Anisotropy, Diffusion regime, Radiative Transfer Equations, Equipartition time

1. Introduction

Modeling of the multiple scattering and diffusion of elastic waves propagating through randomly heterogeneous media via kinetic approaches has received considerable attention in the last few decades. In the stochastic scattering regime, where the correlation length ℓ_c of the heterogeneities of the medium is of the same order of magnitude as the dominant wavelength λ ($\ell_c/\lambda \sim 1$), the propagation length L is much larger than the wavelength ($L/\lambda \gg 1$), and the variance ν^2 of the heterogeneous properties is small ($\nu^2 \ll 1$), the radiative transfer equations (RTE) describe the spatio-temporal evolution of the wave vector dependent energy density of the waves as well as their state of polarization [1, 2, 3, 4, 5, 6, 7]. These RTE have been used to model the propagation of waves in geophysical media, polycrystalline media and concrete [5, 8, 9, 10, 11]. At long lapse time, these equations can be shown to converge to diffusion equations, through an equilibration of the energy into the different modes of propagation (P and S plane waves modes in all directions in the case of wave propagation in unbounded elastic media). This property of equipartition actually appears before diffusion sets in [12, 13], and can be used to infer parameter values of the underground [14, 15, 16, 17, 18, 19, 20].

In most of these approaches, the mechanical behavior is assumed locally isotropic, which means that the constitutive tensor $C(\mathbf{x})$ relating stresses and strains in the elastic wave equation is assumed isotropic in every point in space. It is hence fully characterized by only two parameters (Lamé coefficients for instance). It is also assumed that the material properties fluctuate around an isotropic average, so that the relevant modal energies at the macro-scale are P- and S-energy densities. Nevertheless, this property of local isotropy is not appropriate for many materials, even in the

*shahram.khazaie@univ-nantes.fr

case when the macro-scale behavior might be indeed isotropic. Polycrystals, for instance [21, 22, 23, 24, 2, 5], are composed of assemblies of grain of monocrystals whose behavior is anisotropic, with an orientation that varies from grain to grain. If the grains have no preferred orientation (uniform distribution of orientations), the polycrystal is said to be texture-less [25] and its macroscopic behavior is statistically isotropic. Similar phenomena can be observed in concrete and geophysical materials for example, where individual fractures may induce locally anisotropic behavior while the global behavior would remain isotropic if a dense network of fractures with uniformly random orientations is considered.

In the case of anisotropic materials, Turner [8] derived the RTEs of elastic waves in a transversely isotropic heterogeneous medium. More recently, Baydoun et al. [26] derived the RTEs of elastic waves in a general anisotropic case, where both the background and the fluctuations may be anisotropic. Two main difficulties arise when dealing with general anisotropic media: (i) the number of fluctuating parameters increases with respect to the isotropic case (253 (cross-) power spectral densities (PSDs) must be specified in general for triclinic materials), and (ii) the eigenvectors of the acoustic tensor are not known in general in closed form so that analytical formulations of the RTEs are more difficult to handle. The latter issue only exists for globally anisotropic materials and disappears for locally anisotropic materials with isotropic background because the eigenvectors that are required for the derivation of the RTE are those of the background material. Also, the former issue is simplified when stronger symmetries are considered. For instance, cubic anisotropy only introduces one additional parameter with respect to elasticity, so that only 10 PSDs must be specified.

In [27], numerical simulations seemed to indicate that local anisotropy of a material favored a quicker transition to an equipartition regime, but this was never confirmed theoretically, nor through extensive numerical investigations. The objective of this paper is to challenge this conclusion for a particular texture-less anisotropic material, for which local behavior is cubic. The equipartition time for such a material is therefore derived analytically (Section 3.3), using a particular parameterization (Section 2) and theoretical results of Baydoun et al. [26] for scattering cross-sections (Section 3 and Appendix A). The formula obtained is then compared to the results of numerical simulations of wave propagation in a set of random media with different statistical properties, and to results in the isotropic case (Section 4). Both analytical and numerical results will show that the observations of [27] were chance observations depending on the particular model of material properties that was chosen then. The rate of convergence towards equipartition will actually be shown to depend directly on the correlation between the anisotropy parameter and the shear parameter, with faster convergence for positive correlation.

2. Elastic wave propagation in a randomly heterogeneous medium

In this section, we briefly introduce some general concepts related to the propagation of elastic waves in 3D random media. Random models of the mechanical properties are also introduced.

2.1. Wave equation and mechanical parameters

In non-dissipative elastic media in which the energy losses due to viscosity, friction and radiation are neglected, the displacement vector $\mathbf{u}(\mathbf{x}, t)$ is governed by the equation of motion as:

$$\rho \frac{\partial^2}{\partial t^2} \mathbf{u}(\mathbf{x}, t) - \nabla_{\mathbf{x}} \cdot (C(\mathbf{x}) : \nabla_{\mathbf{x}} \otimes \mathbf{u}(\mathbf{x}, t)) = S(\mathbf{x}_0, t), \qquad (\mathbf{x}, t) \in \Omega \times \mathbb{R}^+ \tag{1}$$

in which $\mathbf{x}$ and t denote the space and time, S is a point source at $\mathbf{x}_0$ and $\Omega \subseteq \mathbb{R}^3$ is the propagation medium. In geological media, the coefficient of variation of the density is observed to be significantly less than that of the phase velocities (or equivalently the elastic moduli) [28]. Consequently, the mass density of geological media is often considered as constant [20]. For the sake of simplicity, we assume throughout that the density is constant (i.e. $\rho(\mathbf{x}) = \rho \in \mathbb{R}^+$). The medium is characterized by a local fourth-order elasticity tensor $C(\mathbf{x}) = C_{ijk\ell}(\mathbf{x})$ which varies continuously in space. Using Voigt's notation, the fourth-order elasticity tensor can be represented via a 6×6 symmetric positive-definite matrix [29]. The number of independent parameters to fully describe the stiffness matrix depends on the type of anisotropy [30]. In the general case, so-called triclinic anisotropy, 21 independent parameters are required to fully describe the elasticity matrix.

2.2. Parameterization of the propagation medium

A probabilistic approach will be employed to model the heterogeneous stiffness matrix $C(\mathbf{x})$. The randomly heterogeneous elasticity matrix is decomposed into a (constant) average $C_0 = \mathbb{E}[C(\mathbf{x})]$, where $\mathbb{E}[\cdot]$ denotes ensemble average, and a small-amplitude rapidly-fluctuating random fluctuation:

$$C(\mathbf{x}) = C_0 + \sqrt{\varepsilon}\, C_1\left(\frac{\mathbf{x}}{\varepsilon}\right), \tag{2}$$

in which ε is a small parameter and $\mathbb{E}[C_1(\mathbf{x})]$. The particular scaling ($\sqrt{\varepsilon}$ for the amplitude and $1/\varepsilon$ for the scale of fluctuation) will be discussed in Section 3. As will become apparent in Section 3, the matrices C_0 and C_1 have different contributions to the wave dynamics in the high-frequency regime, and can belong to different symmetry classes. In most papers (see for instance Ryzhik et al. [6]), both of them are assumed isotropic. This simplifies greatly the computations in the upscaling process, but is not always appropriate, as discussed in the introduction. In this paper, we still consider an isotropic background, but anisotropic fluctuations (of cubic type).

Being isotropic and constant, the background medium is represented by the following elasticity tensor, in terms of its positive eigenvalues κ_0 (bulk modulus) and μ_0 (shear modulus):

$$[C_0]_{ijk\ell} = \kappa_0 \delta_{ij}\delta_{k\ell} + \mu_0\left(\delta_{ik}\delta_{j\ell} + \delta_{i\ell}\delta_{jk} - \frac{2}{3}\delta_{ij}\delta_{k\ell}\right), \tag{3}$$

in which δ_{ij} is Kronecker's delta ($\delta_{ij} = 1$ if $i = j$, and $\delta_{ij} = 0$ if $i \neq j$). Note that the background is assumed homogeneous for simplicity, but fluctuations that are slow with respect to ε can actually be considered without difficulty [6]. The Voigt representation of the average is:

$$C_0 = \frac{1}{3}\begin{bmatrix} 3\kappa_0 + 4\mu_0 & 3\kappa_0 - 2\mu_0 & 3\kappa_0 - 2\mu_0 & 0 & 0 & 0 \\ 3\kappa_0 - 2\mu_0 & 3\kappa_0 + 4\mu_0 & 3\kappa_0 - 2\mu_0 & 0 & 0 & 0 \\ 3\kappa_0 - 2\mu_0 & 3\kappa_0 - 2\mu_0 & 3\kappa_0 + 4\mu_0 & 0 & 0 & 0 \\ 0 & 0 & 0 & 3\mu_0 & 0 & 0 \\ 0 & 0 & 0 & 0 & 3\mu_0 & 0 \\ 0 & 0 & 0 & 0 & 0 & 3\mu_0 \end{bmatrix}. \tag{4}$$

Having cubic anisotropy, the fluctuation can be represented by the following tensor [31], using 3 real-valued eigenvalues $\phi_i(\mathbf{x})$ ($i \in \{1, 2, 3\}$):

$$[C_1(\mathbf{x})]_{ijk\ell} = (\phi_1(\mathbf{x}) + 2\phi_2(\mathbf{x}))\delta_{i\ell}\delta_{jk} + (\phi_1(\mathbf{x}) - \phi_2(\mathbf{x}))\left(\delta_{ij}\delta_{k\ell} - \delta_{i\ell}\delta_{jk}\right) + \phi_3(\mathbf{x})\delta_{ik}\delta_{j\ell}. \tag{5}$$

In order to simplify the comparison of cubic anisotropy with isotropy, we adopt the following parameterization of the eigenvalues : $\kappa_1(\mathbf{x}) = \phi_1(\mathbf{x})$ (with $\kappa_0 + \kappa_1 > 0$), $\mu_1(\mathbf{x}) = \phi_3(\mathbf{x})$ (with $\mu_0 + \mu_1 > 0$) and $\mathcal{A}(\mathbf{x}) = 3\phi_2(\mathbf{x}) - 2\phi_3(\mathbf{x})$ (with $\mathcal{A} > -2(\mu_0 + \mu_1)$). Finally:

$$[C_1(\mathbf{x})]_{ijk\ell} = (\mu_1 + \mathcal{A})\delta_{i\ell}\delta_{jk} + \left(\kappa_1 - \frac{2}{3}\mu_1 - \frac{1}{3}\mathcal{A}\right)\delta_{ij}\delta_{k\ell} + \mu_1\delta_{ik}\delta_{j\ell}, \tag{6}$$

and the Voigt representation of the fluctuation is:

$$C_1(\mathbf{x}) = \frac{1}{3}\begin{bmatrix} 3\kappa_1 + 4\mu_1 + 2\mathcal{A} & 3\kappa_1 - 2\mu_1 - \mathcal{A} & 3\kappa_1 - 2\mu_1 - \mathcal{A} & 0 & 0 & 0 \\ 3\kappa_1 - 2\mu_1 - \mathcal{A} & 3\kappa_1 + 4\mu_1 + 2\mathcal{A} & 3\kappa_1 - 2\mu_1 - \mathcal{A} & 0 & 0 & 0 \\ 3\kappa_1 - 2\mu_1 - \mathcal{A} & 3\kappa_1 - 2\mu_1 - \mathcal{A} & 3\kappa_1 + 4\mu_1 + 2\mathcal{A} & 0 & 0 & 0 \\ 0 & 0 & 0 & 3\mu_1 & 0 & 0 \\ 0 & 0 & 0 & 0 & 3\mu_1 & 0 \\ 0 & 0 & 0 & 0 & 0 & 3\mu_1 \end{bmatrix}. \tag{7}$$

Note that κ_1 and μ_1 can be analyzed as fluctuations (normalized by $\sqrt{\varepsilon}$) of the bulk and shear moduli around their averages κ_0 and μ_0 and $\mathcal{A}$ is a measure of the distance from isotropy. In particular, the behavior of the material is isotropic everywhere whenever $\mathcal{A} = 0$.

The three parameters $\kappa_1(\mathbf{x})$, $\mu_1(\mathbf{x})$ and $\mathcal{A}(\mathbf{x})$ are modeled as correlated zero-mean random functions. The spatial correlation function (CF) of the different pairs of random functions are denoted as $R_{\kappa\kappa}(\mathbf{x},\mathbf{x}')$, $R_{\kappa\mu}(\mathbf{x},\mathbf{x}')$, $R_{\kappa\mathcal{A}}(\mathbf{x},\mathbf{x}')$, $R_{\mu\mu}(\mathbf{x},\mathbf{x}')$, $R_{\mu\mathcal{A}}(\mathbf{x},\mathbf{x}')$ and $R_{\mathcal{A}\mathcal{A}}(\mathbf{x},\mathbf{x}')$. For instance, the second CF is defined as $R_{\kappa\mu}(\mathbf{x},\mathbf{x}') = \mathbb{E}[\kappa_1(\mathbf{x})\mu_1(\mathbf{x}')]$, and the others likewise. It is assumed for simplicity that all CF are statistically isotropic, in the sense that they are all 1D functions of the distance between the two points considered. Classically, these CFs are modeled using kernel functions $\tilde{R}$, correlation length ℓ and variance ν^2. For instance $R_{\kappa\mu}(\mathbf{x},\mathbf{x}') = \nu^2_{\kappa\mu}\tilde{R}_{\kappa\mu}(|\mathbf{x}-\mathbf{x}'|/\ell_{\kappa\mu})$. The correlation length specifies the length scale over which the random function decorrelates significantly and can be seen as the typical size of the heterogeneities. This parameter for the second CF is defined for instance as:

$$\ell_{\kappa\mu} = \frac{2}{R_{\kappa\mu}(0)}\int_{\mathbb{R}^+} R_{\kappa\mu}(r)\mathrm{d}r, \tag{8}$$

and the other correlation lengths likewise. The (cross-) power spectral density functions (PSDF) $\Phi(\psi = |\mathbf{p}|\ell)$ are then defined as the Fourier transform of the kernels of the CFs $\tilde{R}(\eta = |\mathbf{x}-\mathbf{x}'|/\ell)$, in which $\mathbf{p}$ is the Fourier transform relative of $\mathbf{x}-\mathbf{x}'$.

In the analysis and the numerical tests presented in this paper, we will consider five different examples of correlation kernels. They are representative of the models used in the literature and present a wide range of behaviors, with lower or higher frequency content for the same correlation length (in the sense of Eq. (8)) [32, 33]. These examples are summarized in Table 1:

Table 1: Definitions of the normalized correlation models.

Correlation model	Normalized CF $R(\eta)/R(0)$	Normalized PSDF $\Phi(\psi)/R(0)$
Exponential	$\exp(-2\eta)$	$\frac{1}{8\pi^2\left(1+\frac{\psi^2}{4}\right)^2}$
Power-law	$\frac{1}{\left(1+\frac{\pi^2\eta^2}{4}\right)^2}$	$\frac{1}{\pi^4}\exp\left(-2\frac{\psi}{\pi}\right)$
Gaussian	$\exp(-\pi\eta^2)$	$\frac{1}{8\pi^3}\exp\left(-\frac{\psi^2}{4\pi}\right)$
Triangular	$\frac{12(2-2\cos(2\pi\eta)-(2\pi\eta)\sin(2\pi\eta))}{(2\pi\eta)^4}$	$\frac{3}{8\pi^4}\left(1-\frac{\psi}{2\pi}\right)\mathrm{H}\left(2\pi-\psi\right)$
Low-pass white noise	$\frac{3\left(\sin\left(\frac{3\pi}{2}\eta\right)-\frac{3\pi}{2}\eta\cos\left(\frac{3\pi}{2}\eta\right)\right)}{\left(\frac{3\pi}{2}\eta\right)^3}$	$\frac{2}{9\pi^4}\mathrm{H}\left(\frac{3\pi}{2}-\psi\right)$

2.3. Propagation modes

We will see in the next section that energy is transported by modes of the background medium. Since we consider texture-less materials in this paper, the background medium is isotropic, as in Eq. (3). In that case, there are two different propagation modes which will be denoted by $\{\mathrm{P},\mathrm{S}\}$, for the compressional (P) and shear (S) waves. The phase velocities are $v_\mathrm{P} = \sqrt{(\kappa_0+(4/3)\mu_0)/\rho}$ and $v_\mathrm{S} = \sqrt{\mu_0/\rho}$ and the dispersion relations are $\omega^2_\mathrm{P}(\mathbf{k}) = v^2_\mathrm{P}\mathrm{k}^2$ and $\omega^2_\mathrm{S}(\mathbf{k}) = v^2_\mathrm{S}\mathrm{k}^2$. The polarization of the P wave is $\hat{\mathbf{k}} = \mathbf{k}/\mathrm{k}$ where $\mathrm{k} = |\mathbf{k}|$ while that of the S wave spans the two-dimensional plane orthogonal to $\hat{\mathbf{k}}$. There are therefore actually two S waves.

3. Energy transport and equipartition in texture-free anisotropic media

3.1. Radiative transfer equations

In a weakly heterogeneous scattering regime ($\ell_c \sim \lambda$, $L \gg \lambda$ and $\nu^2 \ll 1$), a transport regime occurs when the elastic waves propagate through a typical realization of the random medium described in Section 2.2. In this regime, the spatio-temporal evolution of the ensemble-averaged wave energy densities are described via the so-called radiative transfer equations (RTE, see for instance [34] for details). The RTEs are energy conservation equations corresponding to each of the propagation modes. They consider the full vector nature of the waves along with all possible mode conversions during scattering processes. Using a kinetic approach, transport equations of elastic waves were first

derived in the weakly heterogeneous scattering regime for locally isotropic randomly heterogeneous materials by employing a multiscale expansion of the Wigner transform of the wave field [6]. Recently, Baydoun et al. [26] extended these RTEs to the case of locally anisotropic random media via kinetic modeling of multiple scattering and using the spatio-temporal Wigner transforms and their interpretation in terms of semiclassical operators. The RTEs of elastic waves for texture-less anisotropic random media write:

$$\frac{\partial a_{\mathrm{P}}(\mathbf{k})}{\partial t} - v_{\mathrm{P}}\hat{\mathbf{k}}\cdot\nabla_{\mathbf{x}}a_{\mathrm{P}}(\mathbf{k}) = \int_{\mathbb{R}^3}\sigma_{\mathrm{PP}}(\mathbf{k},\mathbf{k}')a_{\mathrm{P}}(\mathbf{k}')d\mathbf{k}' - \Sigma_{\mathrm{PP}}(\mathbf{k})a_{\mathrm{P}}(\mathbf{k}) + \int_{\mathbb{R}^3}\sigma_{\mathrm{PS}}(\mathbf{k},\mathbf{k}')[a_{\mathrm{S}}(\mathbf{k}')]d\mathbf{k}' - \Sigma_{\mathrm{SP}}(\mathbf{k})a_{\mathrm{P}}(\mathbf{k}) \tag{9a}$$

$$\frac{\partial [a_{\mathrm{S}}(\mathbf{k})]}{\partial t} - v_{\mathrm{S}}\hat{\mathbf{k}}\cdot\nabla_{\mathbf{x}}[a_{\mathrm{S}}(\mathbf{k})] = \int_{\mathbb{R}^3}\sigma_{\mathrm{SS}}(\mathbf{k},\mathbf{k}')[a_{\mathrm{S}}(\mathbf{k}')]d\mathbf{k}' - \Sigma_{\mathrm{SS}}(\mathbf{k})[a_{\mathrm{S}}(\mathbf{k})] + \int_{\mathbb{R}^3}\sigma_{\mathrm{SP}}(\mathbf{k},\mathbf{k}')a_{\mathrm{P}}(\mathbf{k}')d\mathbf{k}' - \Sigma_{\mathrm{PS}}(\mathbf{k})[a_{\mathrm{S}}(\mathbf{k})] \tag{9b}$$

in which $a_\alpha \cong \mathbb{E}[a_\alpha]$ ($\alpha \in \{\mathrm{P},\mathrm{S}\}$) is the projection of the average Wigner transform, or otherwise said, the specific energy density of the wave mode α in the phase space (position $\times$ wavevector) and $\hat{\mathbf{k}} = \mathbf{k}/\mathrm{k}$. In equations (9), the left hand side corresponds to the total derivative of the energy density a_α and is related to the transport of energy in the homogeneous background medium C_0. The contribution of the foreground C_1 is found on the right hand side in terms of the scattering cross-sections ($\sigma_{\alpha\beta}, \Sigma_{\alpha\beta}$) that depend on the background velocities as well as on the PSDFs of the fluctuations of the components of C_1. When a mode with order of multiplicity higher than 1 exists (as for S waves when the background is isotropic), the energy densities are matrices and equations (9) form a matrix system. With an isotropic background, the body wave energy densities are described via a coupled system of one scalar transport equation and one 2×2 matrix transport equation.

3.2. Scattering cross-sections in texture-free cubic media

In the right hand side of equations (9), the scattering mechanism is described via differential and total scattering cross-sections $\sigma_{\alpha\beta}(\mathbf{k},\mathbf{k}')$ and $\Sigma_{\alpha\beta}(\mathbf{k})$ ($\alpha,\beta \in \{\mathrm{P},\mathrm{S}\}$). The rate at which the incident energy of a β-wave propagating with wave vector $\mathbf{k}'$ is scattered into the energy of an α-wave propagating with wave vector $\mathbf{k}$ is represented by the differential scattering cross-sections $\sigma_{\alpha\beta}(\mathbf{k},\mathbf{k}')$ (with unit m^3/s). For the particular case of a cubic fluctuation around an isotropic background, and homogeneous density, the formulas for the differential scattering cross-sections are derived in Appendix A. For clarity, we report below only the final formulas. The differential scattering cross-section from P-wave to P-wave is

$$\begin{aligned}\sigma^{\mathrm{cubic}}_{\mathrm{PP}}(\mathrm{k},\chi)[\mathbf{I}_1] = \frac{\pi \mathrm{k}^2\ell_c^3}{18\rho^2 v_{\mathrm{P}}^3}\Big[&\Big(9\nu_\kappa^2\Phi_{\kappa\kappa} + 4\nu_\mu^2\Phi_{\mu\mu} + \nu_{\mathcal{A}}^2\Phi_{\mathcal{A}\mathcal{A}} - 12\nu_{\kappa\mu}\Phi_{\kappa\mu} - 6\nu_{\kappa\mathcal{A}}\Phi_{\kappa\mathcal{A}} + 4\nu_{\mu\mathcal{A}}\Phi_{\mu\mathcal{A}}\Big)\\ &+3\chi^2\Big(-4\nu_\mu^2\Phi_{\mu\mu} - \nu_{\mathcal{A}}^2\Phi_{\mathcal{A}\mathcal{A}} + 6\nu_{\kappa\mu}\Phi_{\kappa\mu} - 4\nu_{\mu\mathcal{A}}\Phi_{\mu\mathcal{A}} + 3\nu_{\kappa\mathcal{A}}\Phi_{\kappa\mathcal{A}}\Big) + 9\chi^4\Big(4\nu_\mu^2\Phi_{\mu\mu} + \nu_{\mathcal{A}}^2\Phi_{\mathcal{A}\mathcal{A}} + 4\nu_{\mu\mathcal{A}}\Phi_{\mu\mathcal{A}}\Big)\Big],\end{aligned} \tag{10}$$

in which $\mathbf{I}_n$ is the $n\times n$ identity matrix and all the PSDFs are evaluated at $\mathrm{k}\sqrt{2(1-\chi)}$, where $\mathrm{k} = \omega/v_{\mathrm{P}}$ is the wavenumber corresponding to the scattered P waves and χ is the cosine of the scattering angle, i.e. $\chi = \hat{\mathbf{k}}\cdot\hat{\mathbf{k}}'$. The differential scattering cross-section from S-wave to P-wave is such that

$$\sigma^{\mathrm{cubic}}_{\mathrm{PS}}(\mathrm{k},\chi)[\mathbf{I}_2] = \frac{\pi \mathrm{k}^2\ell_c^3}{2\rho^2 v_{\mathrm{S}}^3}\chi^2\left(1-\chi^2\right)\left(4\nu_\mu^2\Phi_{\mu\mu} + 4\nu_{\mu\mathcal{A}}\Phi_{\mu\mathcal{A}} + \nu_{\mathcal{A}}^2\Phi_{\mathcal{A}\mathcal{A}}\right), \tag{11}$$

wherein all the PSDFs are evaluated at $\mathrm{k}\sqrt{1+K^2-2K\chi}$, where k is again the wavenumber corresponding to the scattered P waves and K is the ratio between the average P to the average S wave speeds, i.e. $K = v_{\mathrm{P}}/v_{\mathrm{S}} = \sqrt{\kappa_0/\mu_0 + 4/3}$. Hence, K depends solely on the background medium properties (κ_0,μ_0). Note that the differential scattering cross-section for the P-to-S mode conversion reads:

$$\mathrm{Tr}\left(\sigma^{\mathrm{cubic}}_{\mathrm{SP}}(\mathbf{k},\mathbf{k}')[\mathbf{I}_1]\right) = \sigma^{\mathrm{cubic}}_{\mathrm{PS}}(\mathbf{k}',\mathbf{k})[\mathbf{I}_2]. \tag{12}$$

Finally, the differential scattering cross-section from S-wave to S-wave is such that

$$\sigma^{\mathrm{cubic}}_{\mathrm{SS}}(\mathrm{k},\chi)[\mathbf{I}_2] = \frac{\pi\nu_\mu^2\mathrm{k}^2\ell_c^3}{2\rho^2 v_{\mathrm{S}}^3}\left(4\chi^4 - 3\chi^2 + 1\right)\Phi_{\mu\mu}\left(\mathrm{k}\sqrt{2(1-\chi)}\right)\mathbf{I}_2, \tag{13}$$

in which $\mathrm{k} = \omega/v_{\mathrm{s}}$ is the wavenumber corresponding to the scattered S waves.

The rate at which the incident energy of a β-wave propagating with wave vector $\mathbf{k}$ is scattered into the energy of an α-wave propagating in any direction is called the total scattering cross-section $\Sigma_{\alpha\beta}(\mathbf{k})$ (with unit 1/s) and related to the differential cross-section through:

$$\Sigma_{\alpha\beta}(\mathbf{k}) = \int_{\mathbb{R}^3} \sigma_{\alpha\beta}(\mathbf{k}, \mathbf{k}')[\mathbf{I}_\beta] \frac{\mathrm{d}\mathbf{k}'}{(2\pi)^3};\ \alpha, \beta \in \{\mathrm{P}, \mathrm{S}\}. \tag{14}$$

where $\mathbf{I}_P = \mathbf{I}_1$ and $\mathbf{I}_S = \mathbf{I}_2$. Although the integration can be performed numerically in all generality, we choose here to consider a slightly simplified setting, in order to obtain more condensed formula. We therefore assume that all PSDFs follow the same functional form $\Phi(\psi)$, and that they differ only through the variances and covariances:

$$\Phi_{\kappa\kappa}(\psi) = \Phi_{\kappa\mu}(\psi) = \Phi_{\kappa\mathcal{A}}(\psi) = \Phi_{\mu\mu}(\psi) = \Phi_{\mu\mathcal{A}}(\psi) = \Phi_{\mathcal{A}\mathcal{A}}(\psi) = \Phi(\psi). \tag{15}$$

This hypothesis is only required for clarity and simplicity of the exposition. Total scattering cross sections for a material with isotropic background (texture-free) and cubic fluctuations are derived with this hypothesis in Appendix A. We report here the S-to-P cross section, which is the most significant for the rest of the paper: the P-to-S total scattering coefficient is:

$$\Sigma_{\mathrm{PS}}^{\mathrm{cubic}}(\mathrm{k}) = \frac{(3\kappa - 4\mu)(4\nu_\mu^2 + 4\nu_{\mu\mathcal{A}} + \nu_{\mathcal{A}}^2)\mathrm{k}^4 \ell_c^3}{24\pi\mu^2\sqrt{\rho\mu}} \int_{-1}^{+1} \chi^2 \left(1 - \chi^2\right) \Phi\left(\mathrm{k}\ell_c \sqrt{1 + K^2 - 2K\chi}\right) \mathrm{d}\chi, \tag{16}$$

The corresponding total scattering cross-section for an isotropic fluctuation $\Sigma_{\mathrm{PS}}^{\mathrm{iso}}(\mathrm{k})$ is obtained for $\mathcal{A} = 0$ so that the integral term is the same for both isotropic and cubic fluctuations. This allows in particular to obtain a very simple expression of the ratio for the S-to-P total scattering cross-sections of cubic and isotropic fluctuations:

$$\frac{\Sigma_{\mathrm{PS}}^{\mathrm{cubic}}(\mathrm{k})}{\Sigma_{\mathrm{PS}}^{\mathrm{iso}}(\mathrm{k})} = \frac{4\nu_\mu^2 + 4\nu_{\mu\mathcal{A}} + \nu_{\mathcal{A}}^2}{4\nu_\mu^2}. \tag{17}$$

This ratio is wavenumber-independent and only depends on the components of the covariance matrix of $(\mu, \mathcal{A})$. This observation will be used in the upcoming analysis.

3.3. Influence of anisotropy on the global equipatition time

At long lapse times and after many scattering events, the waves lose track of their source or initial conditions, and the energy spreads equally over all modes of the system [35, 2, 36, 6, 37, 38]. In our system with only two modes, energy is then equipartitioned between P and S waves at a value which is a function only of the ratio of phase velocities, and independent of position:

$$r = \lim_{t \to +\infty} \frac{\mathcal{E}_{\mathrm{S}}(\mathbf{x}, t)}{\mathcal{E}_{\mathrm{P}}(\mathbf{x}, t)} = 2K^3 = 2\left(\frac{v_{\mathrm{P}}}{v_{\mathrm{S}}}\right)^3, \tag{18}$$

in which $\mathcal{E}_{\mathrm{P}}(\mathbf{x}, t)$ and $\mathcal{E}_{\mathrm{S}}(\mathbf{x}, t)$ are the P and S wave energy densities at point $\mathbf{x}$, defined as:

$$\mathcal{E}_{\mathrm{P}}(\mathbf{x}, t) = \frac{3\kappa(\mathbf{x}) + 4\mu(\mathbf{x})}{6} \left(\nabla \cdot \mathbf{u}(\mathbf{x}, t)\right)^2, \quad \mathcal{E}_{\mathrm{S}}(\mathbf{x}, t) = \frac{\mu(\mathbf{x})}{2} \left(\nabla \times \mathbf{u}(\mathbf{x}, t)\right)^2. \tag{19}$$

Although this equipartition is always eventually reached, it will settle in at different rates depending on the particular medium. This paper is concerned with the rate of convergence towards equipartition, and in particular on the influence of anisotropy on that rate of convergence.

This rate of convergence can be evaluated through the equipartition time, for which a formula was proposed in Trégourès and van Tiggelen [39]:

$$t_{\mathrm{eq}}(\mathrm{k}) = \frac{1}{\Sigma_{\mathrm{PS}}(\mathrm{k}) + \mathrm{Tr}\left(\Sigma_{\mathrm{SP}}(\mathrm{k}K)\right)} = \frac{1}{\Sigma_{\mathrm{PS}}(\mathrm{k})\left(1 + \frac{1}{2K^3}\right)}. \tag{20}$$

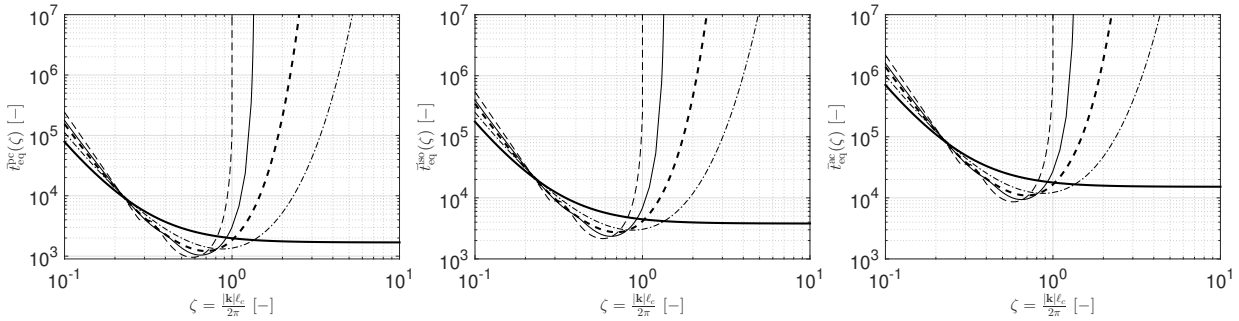

(a) $\nu_{\mu\mathcal{A}} = \nu^2_{\mathcal{A}} = \nu^2_\mu$ (b) $\nu_{\mu\mathcal{A}} = \nu^2_{\mathcal{A}} = 0$ (isotropic) (c) $\nu_{\mu\mathcal{A}} = -\nu^2_{\mathcal{A}} = -\nu^2_\mu$

Figure 1: Normalized global equipartition time as a function of normalized frequency for different values of the correlation of μ and $\mathcal{A}$: $\nu_{\mu\mathcal{A}} = \nu^2_{\mathcal{A}} = \nu^2_\mu$ (left), $\nu_{\mu\mathcal{A}} = \nu_{\mathcal{A}} = 0$ (isotropic,center) and $\nu_{\mu\mathcal{A}} = -\nu^2_{\mathcal{A}} = -\nu^2_\mu$ (right); and for different correlation kernels: exponential (thick solid line), power-law (thin dashed-dotted line), Gaussian (thick dashed line), triangular (thin solid line) and low-pass white noise (thin dashed line).

The equipartition time is therefore inversely proportional to the mean of the P-S and S-P total scattering cross-sections, which is an indicator of the total mixture between the P and S waves [39, 40, 41]. Note that in the formula above, k is the wave number of the P wave, which explains the argument k/K for $\Sigma_{\rm ts}$, which is the wave number of the S wave at the same frequency. Following [33], the normalized (adimensional) form of the equipartition time can be defined as $\bar{t}_{\rm eq} = v_{\rm p} t_{\rm eq}/\ell_c$.

As an illustrative example, consider a heterogeneous material for which the (isotropic) background properties are $\mu_0 = 2\times10^9$ Pa, $\kappa_0 = 3.33\times10^9$ Pa, $\rho = 2000$ kg/m^3, and the fluctuations are such that $\nu^2_\mu = (0.1\times\mu_0)^2 = 4\times10^{16}$ Pa^2 and $\ell_c = 100$ m. Fig. 1 represents the normalized equipartition time as a function of the normalized frequency $\zeta = \mathrm{k}\ell_c/(2\pi)$ (where k is the wave number for the P wave) for different correlation models (see Table 1) and different values of the coefficients of the correlation matrix of μ and $\mathcal{A}$.

Using Eq. (20) and (17), the ratio of equipartition times in isotropic and cubic media can then be obtained as:

$$\frac{t^{\rm iso}_{\rm eq}(\mathrm{k})}{t^{\rm cubic}_{\rm eq}(\mathrm{k})} = \frac{\Sigma^{\rm cubic}_{\rm ts}(\mathrm{k})}{\Sigma^{\rm iso}_{\rm ts}(\mathrm{k})} = \frac{4\nu^2_\mu + 4\nu_{\mu\mathcal{A}} + \nu^2_{\mathcal{A}}}{4\nu^2_\mu}. \tag{21}$$

Clearly, this ratio implies that (cubic) anisotropy does not necessarily imply faster convergence to equipartition, contrarily to what could have been guessed based on the numerical observations in [27]. Indeed, $\nu_{\mu\mathcal{A}}$ can be negative, and reaches its minimum (the semi-positive definiteness of the covariance matrix of $(\mu, \mathcal{A})$ implies that $|\nu_{\mu\mathcal{A}}| \leq \nu_\mu\nu_{\mathcal{A}}$) at $\nu_{\mu\mathcal{A}} = -\nu_{\mathcal{A}}\nu_\mu$. In that case, the ratio of equipartition time is $(1 - \nu_{\mathcal{A}}/(2\nu_\mu))^2 \leq 1$, and convergence is faster with isotropic fluctuations. A similar remark for the positive bound yields:

$$\left(1 - \frac{\nu_{\mathcal{A}}}{2\nu_\mu}\right)^2 \leq \frac{t^{\rm iso}_{\rm eq}(\mathrm{k})}{t^{\rm cubic}_{\rm eq}(\mathrm{k})} \leq \left(1 + \frac{\nu_{\mathcal{A}}}{2\nu_\mu}\right)^2. \tag{22}$$

These bounds are obtained for a perfect anti-correlation and a perfect correlation of μ and $\mathcal{A}$, respectively. Theory therefore predicts that convergence to equipartition can be either faster or slower when local anisotropy is present. Next section aims at illustrating this conclusion on through adequately chosen numerical simulations.

4. Numerical observation of the equipartition regime in a 3D random elastic medium

In this section we investigate the onset of an equipartition regime through the numerical simulations of elastic waves propagating in 3D randomly heterogeneous media in both isotropic and cubic anisotropic materials. These numerical simulations are performed with an implementation of an explicit parallel spectral element solver, which is developed at Institut de Physique du Globe de Paris[1] [42]. The solver has been modified to account for anisotropic fluctuations of the elasticity tensor, and includes a random field generation pre-processor [43, 27].

[1] `http://www.ipgp.fr/~paulcup/RegSEM.html`

Equipartition in a randomly-fluctuating medium with weak heterogeneities settles in only for very large times (see Fig 1). Numerical observation is therefore very complicated because it requires to perform numerical simulations over domains that are *a priori* so large that simulation cannot be performed reasonably (see Khazaie et al. [44] for a detailed discussion). On the one hand, using stronger heterogeneities is not an option because strong localization inhibits transport and equipartition is then not attained. On the other hand, using reflecting boundary conditions impacts the equilibrium between P and S waves so that it might hide the transition to equipartition. Most of this section will therefore be focused on constructing a particular numerical model in which the influence of anisotropy on equipartition can be observed unambiguously.

4.1. Choice of an initial numerical model

A first numerical model is therefore selected to try and understand the implications of truncating the computational domain. The numerical domain is a rectangular cube $\Omega = \{-1500 \text{ m} \leq x, y \leq 1500 \text{ m}; -3000 \text{ m} \leq z \leq 0 \text{ m}\}$, with homogeneous Neumann boundary conditions. The medium has a constant density $\rho = 2000\text{kg/m}^3$, and randomly-fluctuating shear and bulk moduli, with Gamma first-order marginal density, mean values $\mu_0 = 2 \times 10^9\text{Pa}$ and $\kappa_0 = 3.33 \times 10^9\text{Pa}$, so that the average velocities are $v_\text{s} = \sqrt{\mu_0/\rho} = 1000$ m/s and $v_\text{p} = \sqrt{(\kappa_0 + (4/3)\mu_0)/\rho} = 1730$ m/s, and the ratio $K = v_\text{p}/v_\text{s}$ is thus close to $\sqrt{3}$. For simplicity purposes (and because the fluctuation of κ plays little role in the effects we are monitoring), the coefficients of variation of μ and κ are assumed equal to $\delta = 0.1$, so that $\nu_\mu = 2 \times 10^8$ Pa and $\nu_\kappa = 3.33 \times 10^8$ Pa. The anisotropy coefficient $\mathcal{A}$ is assumed perfectly correlated with μ, with $\nu_{\mu\mathcal{A}} = 8 \times 10^{16}$ Pa^2 and $\nu_\mathcal{A} = 4 \times 10^8$ Pa. The correlation structure of the fluctuations of all mechanical parameters is a low-pass white noise (see Table 1), with correlation length $\ell_c = 100$ m. Realizations of the fluctuating constitutive tensor C_1 can be obtained using various schemes [45], and a classical spectral representation approach was chosen in this work [46]. In that technique, the realizations of the random fields are generated in the spectral domain, as sums of cosine functions with increasing frequency and random phases, and with an amplitude controlled by the power spectral density. The random fields generated that way are Gaussian, so their first-order marginal is transformed by local post-processing to the desired first-order marginal density. One of the advantage of this technique is that its computational efficiency can be drastically improved with Fast Fourier Transform algorithms [46]. For very large domains, the algorithm can also be parallelized [47]. A typical realization of the shear modulus of the randomly heterogeneous medium characterized with the aforementioned parameters is depicted in Fig. 2.

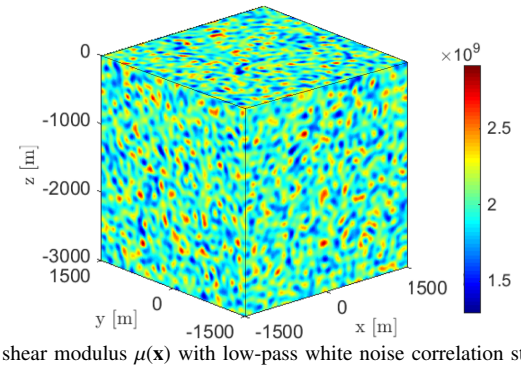

Figure 2: One realization of the random shear modulus $\mu(\mathbf{x})$ with low-pass white noise correlation structure, average $\mu_0 = 2 \times 10^9$Pa, standard deviation $\nu_\mu = 2 \times 10^8$ Pa, and correlation length $\ell_c = 100$m.

A point source is introduced at position $\mathbf{x}_0 = (300, 500, -700)$ m, described in time by a Ricker function (second derivative of a Gaussian function) with a delay of $\tau = 0.3$ s and a central frequency $f_c = 10$ Hz. This implies that the order of magnitude of the wavelengths is close to the correlation length, which ensures (along with the weak heterogeneities and the long propagation path) the validity of the theoretical approach derived in the previous section. Since equipartition is an asymptotic regime independent of the initial source, two different sources will be tested and verified to converge to the same regime. The first type of source is explosive (rotational-free volume force) and introduces at the origin almost only energy in the form of P waves. The second type of source is impulsive (unidirectional volume force pointing downwards), introducing P wave energy along the axis of the force, S-wave energy in all other directions, and on average more S energy than P energy.

4.2. *Observation of equipartition for the initial numerical model*

Based on the simulation of the problem chosen above, local energies can be computed using Eq. (19). Global P and S energies $\overline{\mathcal{E}_\mathrm{p}}$ and $\overline{\mathcal{E}_\mathrm{s}}$ can then be computed as averages over the entire domain of these local energies. For simplicity of comparison with theoretical values of the normalized equipartition time, hereinafter the temporal variations are represented in terms of the normalized time lapse. The latter is defined similar to the normalized equipartition time as $\bar{t} = v_\mathrm{p} t/\ell_c$ where t is the simulation time. As such, in this case we have $\bar{t} = v_\mathrm{p} t/\ell_c \approx 17.3t$. Fig. 3 and 4 display the evolution at different times of the local P and S energies, respectively, along orthogonal planes cutting the computational domain at the position of the source. They give a global picture of the progressive diffraction of the coherent wave front into incoherent energy spreading throughout the domain. Although we only represent the simulation corresponding to the impulsive source, the explosive source yields qualitatively similar plots.

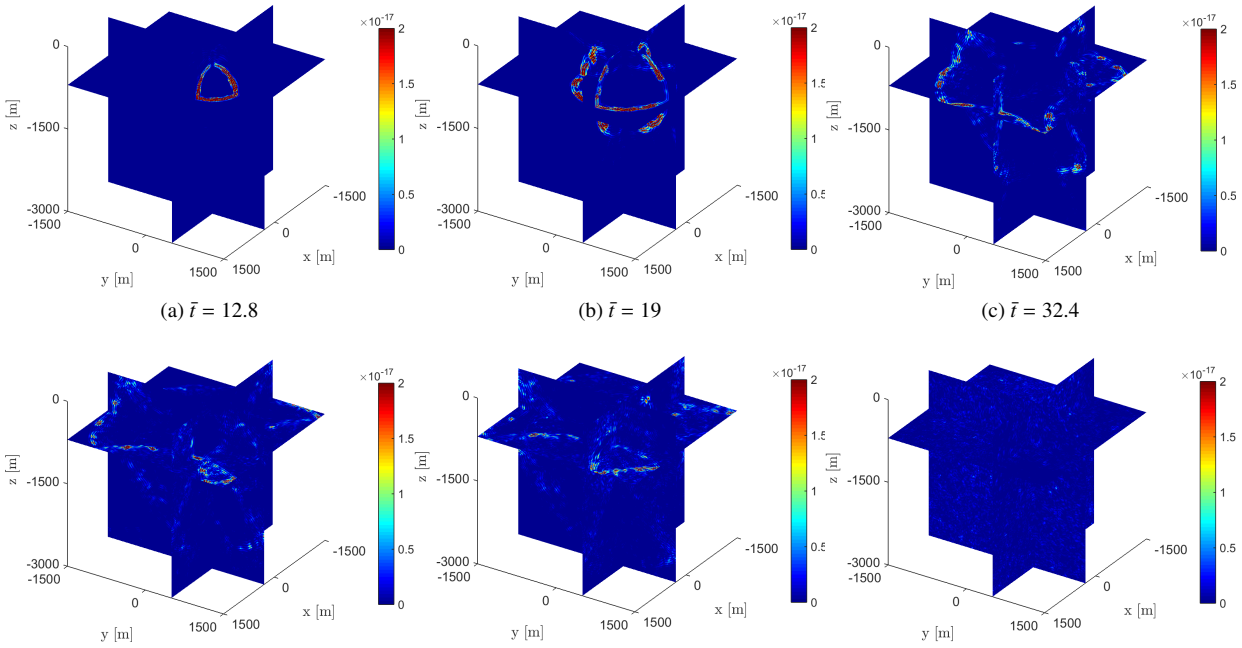

(a) $\bar{t} = 12.8$ (b) $\bar{t} = 19$ (c) $\bar{t} = 32.4$

(d) $\bar{t} = 39.3$ (e) $\bar{t} = 45$ (f) $\bar{t} = 81.8$

Figure 3: S energy density at different normalized times for an impulse source at $\mathbf{x}_0 = (300, 500, -700)$ m and for an anisotropic medium where $\mathcal{A}$ and μ are perfectly correlated via $\mathcal{A} = 2\,(\mu - \mathbb{E}(\mu))$.

Fig. 5 then displays the evolution of the ratio of domain-averaged energy densities for the two different sources. As expected, the ratio of energy densities converges in time to the same equipartition constant independently of the source. Note that this convergence is uniform so that it is observed in each realization of a random medium and not only as an average over different realizations [48, 34]. And the constant obtained at convergence is the value predicted by theory (see Eq. (18), which yields $r \approx 10.36$ for the parameters of that case). Note also that the ratio initially depends strongly on the type of source, with $r > 1$ for the impulsive source and $r \approx 0$ for the explosion, and only becomes independent of the source after long propagation path within the heterogeneous medium. The transition towards equipartition is however not simple and sees many local peaks and valleys (indicated by vertical dashed lines in the right plot of Fig. 5). These are due to the interaction of the different wave fronts with the reflecting boundaries and is analyzed in more detail below.

4.3. *Influence of the reflection at the boundaries*

When a monochromatic P-wave hits a plane boundary with an incidence angle of θ_inc, it is reflected back as both P and S waves with reflecting angles $\theta^\mathrm{P}_\mathrm{ref}$ and $\theta^\mathrm{S}_\mathrm{ref}$. Snell-Descartes law predicts that $\theta^\mathrm{P}_\mathrm{ref} = \theta_\mathrm{inc}$ and $\sin(\theta^\mathrm{S}_\mathrm{ref}) = \sin(\theta_\mathrm{inc})/K$. The reflection coefficients for the P to P mode conversion ($\mathcal{R}_\mathrm{PP}$) and for the P to S mode conversion ($\mathcal{R}_\mathrm{PS}$) can be

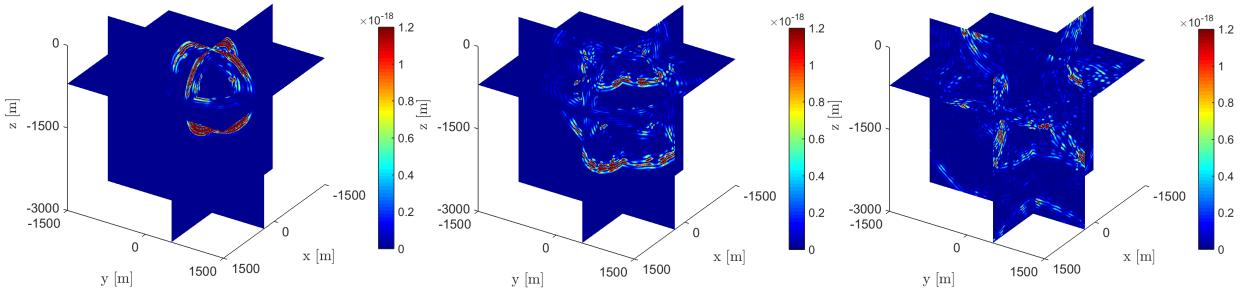

(a) $\bar{t} = 12.8$ (b) $\bar{t} = 19$ (c) $\bar{t} = 32.4$

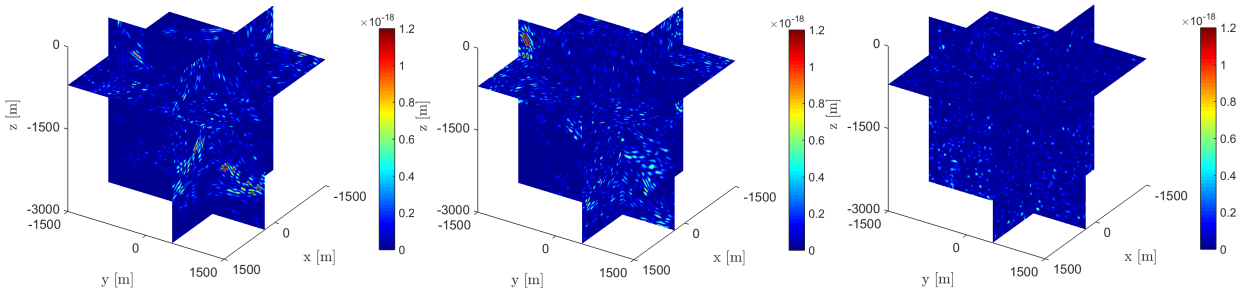

(d) $\bar{t} = 39.3$ (e) $\bar{t} = 45$ (f) $\bar{t} = 81.8$

Figure 4: P energy density at different normalized times for an impulse source at $\mathbf{x}_0 = (300, 500, -700)$ m and for an anisotropic medium where $\mathcal{A}$ and μ are perfectly correlated via $\mathcal{A} = 2(\mu - \mathbb{E}(\mu))$.

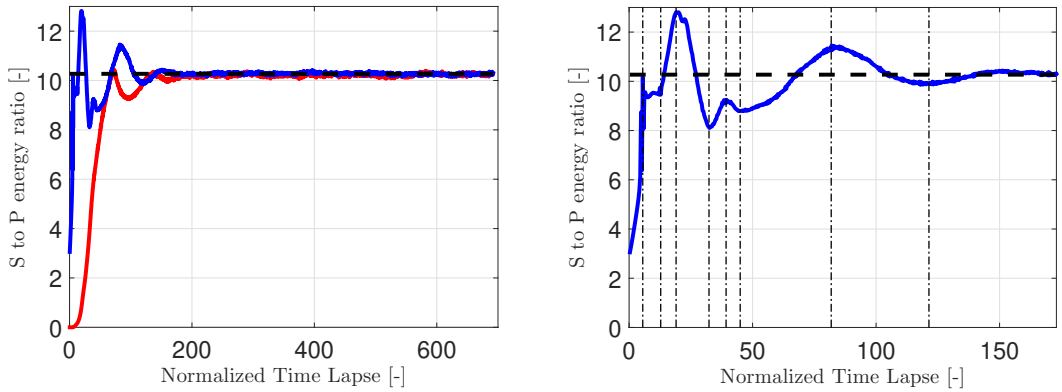

Figure 5: Evolution of the ratio of energy densities of S and P waves in terms of the normalized time lapse $\bar{t}$ for $K = \sqrt{3}$ and two different sources: explosion (red line) and impulsive (blue line). The right plot displays a zoom on the first 10 seconds ($\bar{t}_{\max} = 173$) for the impulsive load. The horizontal dashed line indicates the theoretical value of the equipartition constant, given by Eq. (18). The vertical dashed lines in the right plot indicate local peaks and valleys of the ratio of energy densities.

computed analytically [49, 50]:

$$\begin{cases} \mathcal{R}_{\mathrm{PP}} = \dfrac{\sin(2\theta_{\mathrm{inc}})\sin(2\theta^{\mathrm{P}}_{\mathrm{ref}}) - K^2\cos^2(2\theta^{\mathrm{P}}_{\mathrm{ref}})}{\sin(2\theta_{\mathrm{inc}})\sin(2\theta^{\mathrm{P}}_{\mathrm{ref}}) + K^2\cos^2(2\theta^{\mathrm{P}}_{\mathrm{ref}})} \\ \mathcal{R}_{\mathrm{PS}} = \dfrac{2\sin(2\theta_{\mathrm{inc}})\cos(2\theta^{\mathrm{S}}_{\mathrm{ref}})}{\sin(2\theta_{\mathrm{inc}})\sin(2\theta^{\mathrm{S}}_{\mathrm{ref}}) + K^2\cos^2(2\theta^{\mathrm{S}}_{\mathrm{ref}})} \end{cases} \tag{23}$$

When the incoming wave is an S-wave with incidence angle θ_{inc}, a P-wave is reflected at angle $\sin(\theta^{\text{P}}_{\text{ref}}) = K\sin(\theta_{\text{inc}})$ and an S-wave is reflected at angle $\theta^{\text{S}}_{\text{ref}} = \theta_{\text{inc}}$. The reflection coefficients are [49, 50]:

$$\begin{cases} \mathcal{R}_{\text{SP}} = \dfrac{-2K^2\sin(2\theta_{\text{inc}})\cos(2\theta_{\text{inc}})}{\sin(2\theta_{\text{inc}})\sin(2\theta^{\text{P}}_{\text{ref}}) + K^2\cos^2(2\theta_{\text{inc}})} \\ \mathcal{R}_{\text{SS}} = \dfrac{\sin(2\theta_{\text{inc}})\sin(2\theta^{\text{S}}_{\text{ref}}) - K^2\cos^2(2\theta^{\text{S}}_{\text{ref}})}{\sin(2\theta_{\text{inc}})\sin(2\theta^{\text{S}}_{\text{ref}}) + K^2\cos^2(2\theta^{\text{S}}_{\text{ref}})} \end{cases} \tag{24}$$

Here the reflection coefficients are defined as the ratio between the amplitudes of the reflected and the incident waves. For an incident S wave, since $\theta_{\text{ref}} = \sin^{-1}(K\sin\theta_{\text{ref}})$, there is a critical incidence angle beyond which the reflection occurs along the boundary. This critical incidence angle is $\theta^{\text{c}}_{\text{inc}} = \sin^{-1}(K^{-1})$ and thus for instance $K = \sqrt{3}$ yields a critical angle of about 35°. Fig. 6 shows the influence of the incidence angle and the ratio K on reflection coefficients for the P-to-S and S-to-P mode conversions, depending on the incident angle.

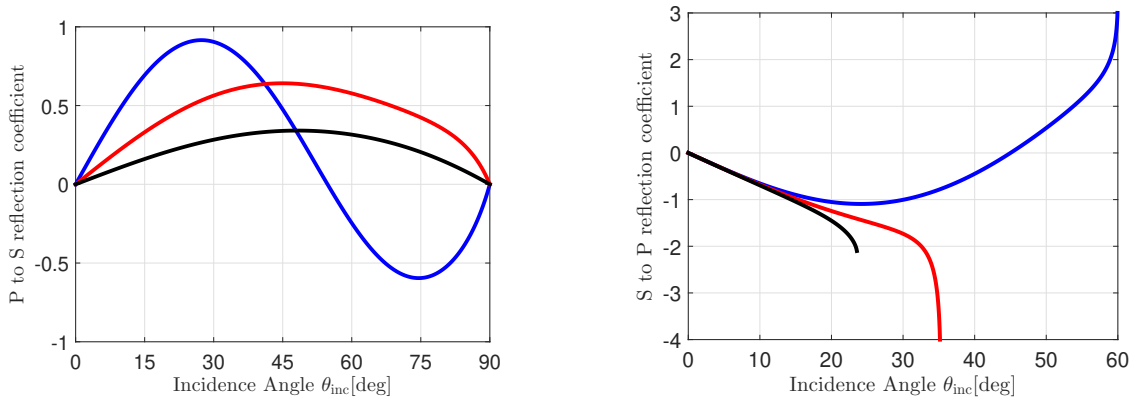

(a) $R_{\text{PS}}(\theta_{\text{inc}})$ for different K (b) $R_{\text{SP}}(\theta_{\text{inc}})$ for different K

Figure 6: Reflection coefficients for the P-to-S and S-to-P mode conversions in terms of the incident angle θ_{inc} for different values of the ratio K: $K = 2.5$ (black line), $K = \sqrt{3}$ (red line) and $K = \sqrt{4/3}$ (blue line).

Coming back to the analysis of the rise of equipartition in Fig. 5, the influence of the interaction of the different coherent waves with the boundaries can be better understood by comparing the time of the dashed lines and the plots in Fig. 3 and 4. For instance, around time $t \approx 0.7 - 0.8$ s ($\bar{t} \in [12.11, 13.8]$), the coherent P waves emitted at the source begin interacting with the boundary, while the coherent S waves arrive at the boundary around $t \approx 1 - 1.1$ s ($\bar{t} \in [17.3, 19]$). While the former implies an increase of the S-to-P energy ratio (through conversion of part of the P-energy into S-energy), the latter marks the beginning of a decrease of the S-to-P energy ratio (through conversion of part of the S-energy into P-energy). Later reflections are less salient because the wave fronts are less coherent (the energy is spread more widely in space and propagation direction), and also because the source is not located at the center of the box, so that interactions do not take place simultaneously on all boundaries.

4.4. Design of a new model with minimized mode conversion at the boundary

As the objective of this section is to observe equipartition arise from the heterogeneity of the medium only, and not because of mode conversions at the boundaries, a modification of the numerical model of Section 4.1 is therefore proposed. That modification is chosen so as to minimize mode conversions at the boundaries, hence increasing the relative influence of the heterogeneities on equipartition. For instance, with an explosion that creates an initial majority of P waves, it is desirable to minimize the P-to-S conversion. Thanks to the left plot of Fig. 6, it is then chosen to consider a larger value of the velocity ratio at $K = 2.5$. The previous numerical model is therefore modified by considering $\kappa_0 = 9.8333 \times 10^9$ Pa and $v_{\text{p}} = 2500$ m/s. With the rest of the setting unchanged, the new expected value of the equipartition ratio is now $r \approx 31.25$, and it is indeed observed numerically in Fig. 7 which shows the variation of the energy density ratio in terms of the normalized simulation time. Compared to Fig. 5, it is clear that the local

peaks have vanished, and transition to equipartition is now smoother. In order to investigate the influence of the size of the domain on the time to equipartiton, three different domains are considered, all cubes, with respective sides of 2500 m, 3000 m and 3500 m. As expected, the existence of the boundary increases the rate of mixing of modes so that equipartition takes place faster in a smaller domain, because waves interact more often with the boundaries. Furthermore, since the theoretical model only discusses the influence on equipartition of the bulk heterogeneities, there is a discrepancy with the numerical model. Hence, the time to equipartition in a bounded domain is expected to be smaller than the theoretical value.

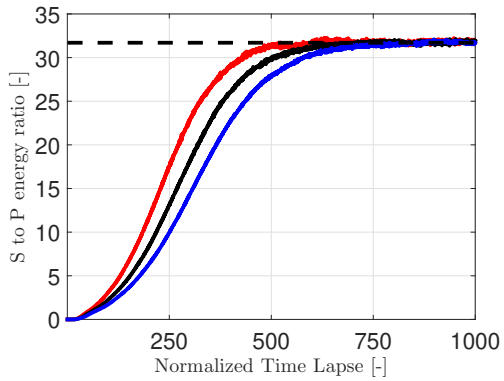

Figure 7: Evolution of the ratio of energy densities of S and P waves for $K = 2.5$ and an explosive source in terms of the normalized time lapse for three different medium sizes. Cubes with respective sides of 2500 m (red line), 3000 m (black line) and 3500 m (blue line). The horizontal dashed line indicates the theoretical value of the equipartition constant, given by Eq. 18.

In order to investigate further the influence of the boundaries on the results, and in particular to make sure that transition is not controlled by the boundaries but rather by the bulk heterogeneities, we design one last numerical simulation with a homogeneous medium excited with the same explosion source. All parameters are the same as above, except that the fluctuations of the properties vanish. The domain is a cube whose sides are 3000 m long. Figure 8 shows the variation of the energy ratio in terms of the normalized time lapse. Initially, the explosion source creates the P waves so that the ratio vanishes until approximately a normalized time of 17. After that time, interactions with the boundaries take place (over a long time because the explosion is not centered) and the ratio increases. Not however that, contrarily to previous simulations, the theoretical ratio (close to 31) is not reached. A slow convergence is observed, which indicates, as expected, that the boundaries do influence transition to equipartition. However, that transition provoked by the boundaries seems much smaller than that provoked by the heterogeneities. The proposed design for the numerical model seems therefore appropriate to study numerically the influence of anisotropy on equipartition.

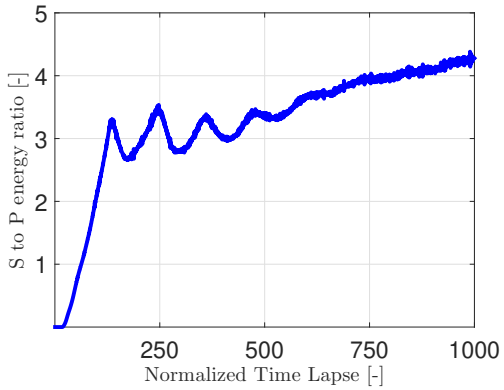

Figure 8: Evolution of the ratio of energy densities of S and P waves for $K = 2.5$ and an explosive source in terms of the normalized time lapse for a cube whose sides are 3000 m long.

For the rest of this section, explosive sources will be considered with this ratio of velocities $K = 2.5$. For all

the simulations to be discussed below, the set of numerical and mechanical parameters will be kept identical to those of this section, except for the anisotropy parameter $\mathcal{A}$ that will evolve to analyze the influence of anisotropy on equipartition.

4.5. Comparison between isotropic and cubic anisotropic media

Finally, we can turn to the numerical confirmation of the influence of anisotropy on the rate of convergence to equipartition. Using the numerical model above, different choices of the anisotropy parameter $\mathcal{A}$ are introduced:

1. with $\mathcal{A} = 2\mu_1$, the variances are $v_{\mathcal{A}}^2 = 4v_\mu^2$ and $v_{\mu\mathcal{A}} = 2v_\mu^2$ and a rapid rise of equipartition is observed, slightly faster than in the isotropic case;
2. with $\mathcal{A} = \mu_1$, the variances are $v_{\mathcal{A}}^2 = v_{\mu\mathcal{A}} = v_\mu^2$ and equipartition comes in slightly slower than for the previous case, and slightly faster than for the isotropic case;
3. with $\mathcal{A} = 0$, the isotropic case is retrieved;
4. with $\mathcal{A} = -\mu_1$, the variances are $v_{\mathcal{A}}^2 = v_\mu^2$ and $v_{\mu\mathcal{A}} = -v_\mu^2$ and equipartition is slower than in the isotropic case, as expected;
5. with $\mathcal{A} = -2\mu_1$, the lower bound of Eq. (21) is attained with $v_{\mathcal{A}}^2 = 4v_\mu^2$ and $v_{\mu\mathcal{A}} = -2v_\mu^2$ and equipartition time theoretically diverges.

The ratios of global S-to-P energies are plotted in Fig. 9 in terms of the normalized time lapse $\bar{t}$ for different cases introduced above. Note that the left and right plots correspond to medium with sides 3000 m and 3500 m, respectively. Qualitatively, the results obtained through numerical experiments do confirm the theoretical results obtained in the previous section. Quantitative comparison cannot be considered because the boundaries do eventually influence the rate of convergence, even though this influence has been minimized. Note that for the last case, which yields theoretically an infinite equipartition time, the numerical simulation was stopped before full convergence although equipartition did seem to eventually arise.

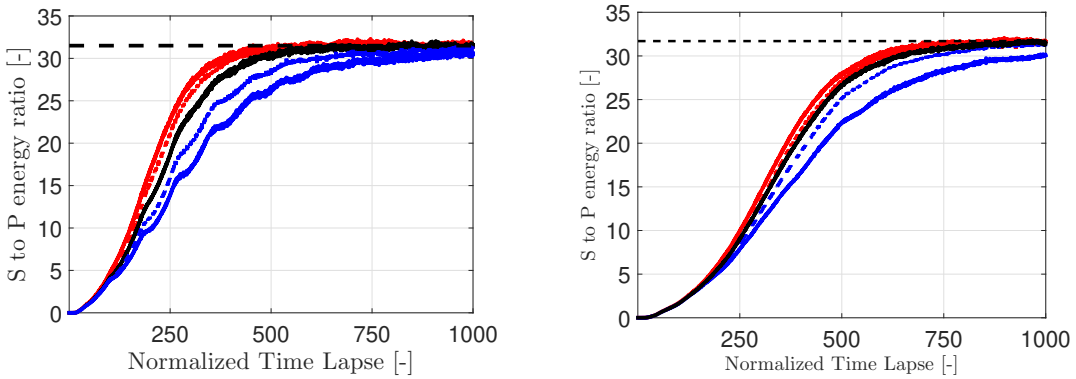

Figure 9: Variation of the S to P wave energy ratio for an explosion source and different values of the ratio $c = v_{\mathcal{A}}/v_\mu$ in terms of the normalized time lapse: $c = 2$ (solid red line), $c = 1$ (dashed red line), $c = 0$ (isotropic, solid black line), $c = -1$ (dashed blue line), $c = -2$ (solid blue line). The horizontal dashed line indicates the theoretical value of the equipartition constant, given by Eq. 18. The left and right plots correspond to the cubes with sides 3000 m and 3500 m, respectively.

5. Conclusion

This paper discussed the importance of local anisotropy on the onset of the equipartition regime, even when the medium is statistically isotropic (texture-free). For a cubic local anisotropy, the full set of differential and total scattering cross sections have been derived and a formula has been proposed for the time to equipartition. Relatively to the isotropic case, this equipartition time was shown to be strongly influenced by the correlation between the shear modulus $\mu(\mathbf{x})$ and the anisotropy parameter $\mathcal{A}(\mathbf{x})$ for locally cubic media. Note that a strong hypothesis was introduced in the analysis, which is that all random mechanical parameters have the same correlation structure, even though their variance and cross-correlation differ. This hypothesis was necessary in order to derive simple enough results.

Although numerical issues impeded direct verification of this analytical result in full space, a bounded numerical model was constructed that minimized the influence of boundary conditions on the rise of equipartition. The numerical observation of time to equipartition for different correlations confirms that (i) local anisotropy is influential on the rate of convergence to equipartition; and (ii) positive correlation between the shear modulus $\mu(\mathbf{x})$ and the anisotropy parameter $\mathcal{A}(\mathbf{x})$ favors the rise of equipartition.

Other types of anisotropy could be studied in the same manner, although parameterization would require to introduce more independent random fields for the constitutive tensor. Alternatively, it would be interesting to consider the influence of the anisotropy of the correlation structure, and/or the influence of an anisotropic background. The former case, which is referred to as anisomery in the dedicated literature [51], could be obtained quite easily as an extension of this paper, although parameterization would again have to be addressed. For the latter case, a more profound modification would be necessary because the modes of the background in that case are not simple P and S modes and equipartition takes on a more complex form.

Acknowledgments

This work was performed using HPC resources from the "Mésocentre" computing center of CentraleSupélec and École Normale Supérieure Paris-Saclay and the Centre de Calcul Intensif des Pays de la Loire (CCIPL) in Nantes.

Appendix A. Calculation of differential scattering cross-sections for cubic anisotropic fluctuations

In this appendix, we derive the full set of differential and total scattering cross-sections for the elasticity equation with homogeneous density, isotropic background and cubic fluctuations. The orthonormal eigenvectors of the Christoffel tensor of the background medium define the polarization directions, henceforth denoted as:

$$\mathbf{p}_{\mathrm{P}}(\mathbf{k}) = \hat{\mathbf{k}}, \qquad \mathbf{p}_{\mathrm{S}}(\mathbf{k}) = [\hat{\mathbf{z}}_1(\mathbf{k}), \hat{\mathbf{z}}_2(\mathbf{k})]^T, \tag{A.1}$$

in which the superscript T denotes the transpose operation. Following Baydoun et al. [26], the differential scattering cross-section operator for the general case of anisotropic material behavior corresponding to the β-to-α mode conversion $\sigma_{\alpha\beta}(\mathbf{k}, \mathbf{q})$ reads:

$$\delta(\mathbf{0})(2\pi)^3 \sigma_{\alpha\beta}(\mathbf{k}, \mathbf{q})[a_\beta(\mathbf{q})] = \frac{\pi}{2\omega_\alpha(\mathbf{k})\omega_\beta(\mathbf{q})} \mathbb{E}\left[\mathbf{H}_{\alpha\beta}(\mathbf{k}, \mathbf{k}-\mathbf{q}, \mathbf{q}) a_\beta(\mathbf{q}) \mathbf{H}_{\beta\alpha}(\mathbf{q}, \mathbf{q}-\mathbf{k}, \mathbf{k})\right] \delta\left(\omega_\alpha(\mathbf{k}) - \omega_\beta(\mathbf{q})\right), \tag{A.2}$$

in which $[a_\beta(\mathbf{q})]$ is the incident wave energy density of type $\beta \in \{\mathrm{P}, \mathrm{S}\}$ in phase space, and δ is the Dirac delta distribution. The Dirac delta in the right hand side is related to the conservation of frequency during the scattering process. By contrast, the Dirac delta in the left hand side arises from the definition of the power spectral density of the mechanical properties and will simplify with its counterpart hidden in the the average of product of functions $\mathbf{H}$ (see below, and [26] for more details). In Eq. (A.2) $\mathbf{H}_{\alpha\beta}$ is defined by pre and post multiplication of a 3×3 matrix $\mathbf{H}(\mathbf{k}, \mathbf{p}, \mathbf{q})$ respectively by the polarization vectors $\mathbf{p}^*_\alpha(\mathbf{k})$ and $\mathbf{p}_\beta(\mathbf{q})$, where the star * denotes the conjugate transpose of a complex vector. The matrix $\mathbf{H}(\mathbf{k}, \mathbf{p}, \mathbf{q})$ is defined as $[\mathrm{H}(\mathbf{k}, \mathbf{p}, \mathbf{q})]_{ik} = \rho^{-1} k_j q_\ell [\widehat{C_1}(\mathbf{p})]_{ijk\ell}$, wherein the Einstein implicit summation convention is utlilized which implies that $\mathbf{H}(\mathbf{k}, \mathbf{p}, \mathbf{q}) = \mathbf{H}^*(\mathbf{q}, \mathbf{p}, \mathbf{k})$. When the fluctuation matrix C_1 is cubic, the matrices $\mathbf{H}(\mathbf{k}, \mathbf{p}, \mathbf{q})$ and $\mathbf{H}_{\alpha\beta}(\mathbf{k}, \mathbf{p}, \mathbf{q})$ can be obtained as

$$\mathbf{H}(\mathbf{k}, \mathbf{p}, \mathbf{q}) = \rho^{-1}\left[\left(\frac{3\widehat{\kappa}(\mathbf{p}) - 2\widehat{\mu}(\mathbf{p}) - \widehat{\mathcal{A}}(\mathbf{p})}{3}\right)\mathbf{k}\otimes\mathbf{q} + \widehat{\mu}(\mathbf{p})\mathbf{q}\otimes\mathbf{k} + \widehat{\mu}(\mathbf{p})(\mathbf{k}.\mathbf{q})\mathbf{I_3} + \widehat{\mathcal{A}}(\mathbf{p})\mathrm{diag}(k_1q_1, k_2q_2, k_3q_3)\right] \tag{A.3}$$

and

$$\begin{aligned}\mathbf{H}_{\alpha\beta}(\mathbf{k}, \mathbf{p}, \mathbf{q}) = \rho^{-1}\mathrm{kq}\Bigg[&\left(\frac{3\widehat{\kappa}(\mathbf{p}) - 2\widehat{\mu}(\mathbf{p}) - \widehat{\mathcal{A}}(\mathbf{p})}{3}\right)(\hat{\mathbf{k}}\cdot\mathbf{p}_\alpha(\mathbf{k}))^*(\hat{\mathbf{q}}\cdot\mathbf{p}_\beta(\mathbf{q})) \\ &+\widehat{\mu}(\mathbf{p})\left((\hat{\mathbf{q}}\cdot\mathbf{p}_\alpha(\mathbf{k}))^*(\hat{\mathbf{k}}\cdot\mathbf{p}_\beta(\mathbf{q})) + (\hat{\mathbf{k}}\cdot\hat{\mathbf{q}})(\mathbf{p}^*_\alpha(\mathbf{k})\cdot\mathbf{p}_\beta(\mathbf{q}))\right) + \widehat{\mathcal{A}}(\mathbf{p})\mathbf{p}^*_\alpha(\mathbf{k})\mathrm{diag}(k_1q_1, k_2q_2, k_3q_3)\mathbf{p}_\beta(\mathbf{q})\Bigg].\end{aligned} \tag{A.4}$$

Replacing the definitions for $\mathbf{H}_{\alpha\beta}$ and particularizing for each mode α and β in Eq. (A.2) yields the definition of the differential scattering cross-section for each pair of modes. Then, the total scattering cross-sections is obtained using

$$\Sigma_{\alpha\beta}(\mathbf{k}) = \int_{\mathbb{R}^3} \sigma_{\alpha\beta}(\mathbf{k},\mathbf{k}')[\mathbf{I}_n]\frac{\mathrm{d}\mathbf{k}'}{(2\pi)^3};\ \alpha,\beta \in \{\mathrm{P},\mathrm{S}\}, \tag{A.5}$$

where $\mathbf{I}_n$ is the $n \times n$ identity matrix. In the following subsections, the computations of the differential and total scattering cross-sections are performed for an elastic material with an isotropic background and cubic fluctuations.

Appendix A.1. Calculation of P-P scattering cross-sections

For P-P scattering, we have $\alpha = \beta = \mathrm{P}$ and $\mathbf{p}_{\mathrm{P}}(\mathbf{k}) = \hat{\mathbf{k}}$. Then, $(\hat{\mathbf{k}}\cdot\mathbf{p}_{\mathrm{P}}(\mathbf{k}))^* = \hat{\mathbf{q}}\cdot\mathbf{p}_{\mathrm{P}}(\mathbf{q}) = 1$, $(\hat{\mathbf{q}}\cdot\mathbf{p}_{\mathrm{P}}(\mathbf{k}))^* = \hat{\mathbf{k}}\cdot\mathbf{p}_{\mathrm{P}}(\mathbf{q}) = \mathbf{p}_{\mathrm{P}}^*(\mathbf{k})\cdot\mathbf{p}_{\mathrm{P}}(\mathbf{q}) = \hat{\mathbf{k}}\cdot\hat{\mathbf{q}}$ and $\hat{\mathbf{k}}^T\mathrm{diag}(k_1q_1,k_2q_2,k_3q_3)\hat{\mathbf{q}} = \sum_{j=1}^3 k_j^2q_j^2 = \cos^2\theta = (\hat{\mathbf{k}}\cdot\hat{\mathbf{q}})^2$. Inserting these relations in (A.4) yields:

$$\mathbf{H}_{\mathrm{PP}}(\mathbf{k},\mathbf{p},\mathbf{q}) = \frac{\mathrm{kq}}{3\rho}\left[\left(3\widehat{\kappa}(\mathbf{p}) - 2\widehat{\mu}(\mathbf{p}) - \widehat{\mathcal{A}}(\mathbf{p})\right) + 3(\hat{\mathbf{k}}\cdot\hat{\mathbf{q}})^2\left(2\widehat{\mu}(\mathbf{p}) + \widehat{\mathcal{A}}(\mathbf{p})\right)\right]. \tag{A.6}$$

Inserting this into Eq. (A.2) yields:

$$\begin{aligned}\delta(\mathbf{0})(2\pi)^3\sigma_{\mathrm{PP}}^{\mathrm{cubic}}(\mathbf{k},\mathbf{q})[a_{\mathrm{P}}(\mathbf{q})] = \frac{\pi}{18\nu_{\mathrm{P}}^2}\frac{\mathrm{kq}}{\rho^2}\mathbb{E}\Big\{&\left[\left(3\widehat{\kappa}(\mathbf{k}-\mathbf{q}) - 2\widehat{\mu}(\mathbf{k}-\mathbf{q}) - \widehat{\mathcal{A}}(\mathbf{k}-\mathbf{q})\right) + 3(\hat{\mathbf{k}}\cdot\hat{\mathbf{q}})^2\left(2\widehat{\mu}(\mathbf{k}-\mathbf{q}) + \widehat{\mathcal{A}}(\mathbf{k}-\mathbf{q})\right)\right]\\ &\left[\left(3\widehat{\kappa}(\mathbf{q}-\mathbf{k}) - 2\widehat{\mu}(\mathbf{q}-\mathbf{k}) - \widehat{\mathcal{A}}(\mathbf{q}-\mathbf{k})\right) + 3(\hat{\mathbf{k}}\cdot\hat{\mathbf{q}})^2\left(2\widehat{\mu}(\mathbf{q}-\mathbf{k}) + \widehat{\mathcal{A}}(\mathbf{q}-\mathbf{k})\right)\right]\Big\}a_{\mathrm{P}}(\mathbf{q})\delta\left(\nu_{\mathrm{P}}(\mathrm{k}-\mathrm{q})\right).\end{aligned} \tag{A.7}$$

With no loss of generality, we assume that the scattered wave vector $\mathbf{k}$ lies along a particular direction. The incident and scattered wave vectors and bases are then taken as:

$$\hat{\mathbf{k}} = \begin{pmatrix}0\\0\\1\end{pmatrix}\quad;\quad z^{(1)}(\mathbf{k}) = \begin{pmatrix}1\\0\\0\end{pmatrix}\quad;\quad z^{(2)}(\mathbf{k}) = \begin{pmatrix}0\\1\\0\end{pmatrix} \tag{A.8}$$

$$\hat{\mathbf{q}} = \begin{pmatrix}\sin\theta\cos\phi\\ \sin\theta\sin\phi\\ \cos\theta\end{pmatrix}\quad;\quad z^{(1)}(\mathbf{q}) = \begin{pmatrix}\cos\theta\cos\phi\\ \cos\theta\sin\phi\\ -\sin\theta\end{pmatrix}\quad;\quad z^{(2)}(\mathbf{q}) = \begin{pmatrix}-\sin\phi\\ \cos\phi\\ 0\end{pmatrix} \tag{A.9}$$

We denote additionally $(\hat{\mathbf{k}}\cdot\hat{\mathbf{q}}) = \cos\theta = \chi$. The PSDF of the mechanical properties can be expressed in terms of the mathematical expectation of the product of Fourier transformations of two homogeneous (stationary) random fields $\Xi(\mathbf{x})$ and $\Psi(\mathbf{x})$ as:

$$\mathbb{E}\left[\widehat{\Xi}(\mathbf{p})\widehat{\Psi}(-\mathbf{p})\right] = \delta(\mathbf{0})(2\pi)^3\ell_c^3\nu_{\Xi\Psi}\Phi_{\Xi\Psi}(|\mathbf{p}|), \tag{A.10}$$

in which $\nu_{\Xi\Psi}$ is the correlation coefficient of the random fields and the correlation function is assumed to have an isotropic structure. Hence, from Eq. (A.7) multiplying term by term, taking the mathematical expectation and making use of (A.10) yields:

$$\begin{aligned}\sigma_{\mathrm{PP}}^{\mathrm{cubic}}(\mathrm{q},\chi)[a_{\mathrm{P}}(\mathbf{q})] = \frac{\pi\mathrm{q}^2\ell_c^3}{18\rho^2\nu_{\mathrm{P}}^3}\Big[&\left(9\nu_\kappa^2\Phi_{\kappa\kappa} + 4\nu_\mu^2\Phi_{\mu\mu} + \nu_{\mathcal{A}}^2\Phi_{\mathcal{A}\mathcal{A}} - 12\nu_{\kappa\mu}\Phi_{\kappa\mu} - 6\nu_{\kappa\mathcal{A}}\Phi_{\kappa\mathcal{A}} + 4\nu_{\mu\mathcal{A}}\Phi_{\mu\mathcal{A}}\right)\\ &+3\chi^2\left(-4\nu_\mu^2\Phi_{\mu\mu} - \nu_{\mathcal{A}}^2\Phi_{\mathcal{A}\mathcal{A}} + 6\nu_{\kappa\mu}\Phi_{\kappa\mu} - 4\nu_{\mu\mathcal{A}}\Phi_{\mu\mathcal{A}} + 3\nu_{\kappa\mathcal{A}}\Phi_{\kappa\mathcal{A}}\right) + 9\chi^4\left(4\nu_\mu^2\Phi_{\mu\mu} + \nu_{\mathcal{A}}^2\Phi_{\mathcal{A}\mathcal{A}} + 4\nu_{\mu\mathcal{A}}\Phi_{\mu\mathcal{A}}\right)\Big]a_{\mathrm{P}}(\mathbf{q}),\end{aligned} \tag{A.11}$$

where we used the identity $\delta(ax) = \delta(x)/|a|$ (for any non-zero scalar a) and then $\delta(\mathrm{k}-\mathrm{q})$ or $\mathrm{k} = \mathrm{q}$ implies that the argument of all PSDFs is $|\mathbf{k}-\mathbf{q}| = \sqrt{\mathrm{k}^2+\mathrm{q}^2-2\mathrm{kq}\chi} = \mathrm{q}\sqrt{2(1-\chi)}$ in which $\mathrm{q} = |\mathbf{q}| = \omega/\nu_{\mathrm{P}}$ is the wavenumber of a P mode. Note that we have changed the arguments of the scattering function from $(\mathbf{k},\mathbf{q})$ in Eq. (A.7) to (q,χ) above to insist on the fact that only the norm of the incident (or scattered) vector and the angle between the two vectors are influential.

Selecting $\mathcal{A} = 0$ allows to fall back on the classical P-P differential scattering cross-section for isotropic fluctuations [2, 6, 37, 26]:

$$\sigma_{\mathrm{PP}}^{\mathrm{iso}}(\mathrm{q},\chi)[a_{\mathrm{P}}(\mathbf{q})] = \frac{\pi\mathrm{q}^2\ell_c^3}{18\rho^2\nu_{\mathrm{P}}^3}\left[\left(9\nu_\kappa^2\Phi_{\kappa\kappa} + 4\nu_\mu^2\Phi_{\mu\mu} - 12\nu_{\kappa\mu}\Phi_{\kappa\mu}\right) + 3\chi^2\left(-4\nu_\mu^2\Phi_{\mu\mu} + 6\nu_{\kappa\mu}\Phi_{\kappa\mu}\right) + 36\chi^4\nu_\mu^2\Phi_{\mu\mu}\right]a_{\mathrm{P}}(\mathbf{q}). \tag{A.12}$$

Integration can then be performed following Eq. (A.5) to obtain the total scattering cross section for the P-to-P scattering. Although possible in all generality, we choose here to consider a slightly simplified setting, only to present more condensed formula. We therefore assume that all PSDFs follow the same functional form $\Phi(\psi)$, and that they differ only through the variances and covariances:

$$\Phi_{\kappa\kappa}(\psi) = \Phi_{\kappa\mu}(\psi) = \Phi_{\kappa\mathcal{A}}(\psi) = \Phi_{\mu\mu}(\psi) = \Phi_{\mu\mathcal{A}}(\psi) = \Phi_{\mathcal{A}\mathcal{A}}(\psi) = \Phi(\psi). \tag{A.13}$$

Following Eq. (A.5) with this hypothesis (and $\mathbf{I}_1 = 1$) yields:

$$\Sigma_{\text{PP}}^{\text{cubic}}(\mathrm{q}) = \frac{\mathrm{q}^4\ell_c^3}{72\pi\rho^2 v_{\text{P}}^3}\int_{-1}^{+1}\Big[\Big(9\nu_\kappa^2 + 4\nu_\mu^2 + \nu_{\mathcal{A}}^2 - 12\nu_{\kappa\mu} - 6\nu_{\kappa\mathcal{A}} + 4\nu_{\mu\mathcal{A}}\Big) \\ +3\chi^2\Big(-4\nu_\mu^2 - \nu_{\mathcal{A}}^2 + 6\nu_{\kappa\mu} - 4\nu_{\mu\mathcal{A}} + 3\nu_{\kappa\mathcal{A}}\Big) + 9\chi^4\Big(4\nu_\mu^2 + \nu_{\mathcal{A}}^2 + 4\nu_{\mu\mathcal{A}}\Big)\Big]\,\Phi\left(\mathrm{q}\sqrt{2(1-\chi)}\right)\mathrm{d}\chi, \tag{A.14}$$

Similarly as above, the selection of $\mathcal{A} = 0$ yields the classical P-P total scattering cross-section for isotropic fluctuations:

$$\Sigma_{\text{PP}}^{\text{iso}}(\mathrm{q}) = \frac{\mathrm{q}^4\ell_c^3}{72\pi\rho^2 v_{\text{P}}^3}\int_{-1}^{+1}\Big[\Big(9\nu_\kappa^2 + 4\nu_\mu^2 - 12\nu_{\kappa\mu}\Big) + 3\chi^2\Big(-4\nu_\mu^2 + 6\nu_{\kappa\mu}\Big) + 36\chi^4\nu_\mu^2\Big]\,\Phi\left(\mathrm{q}\sqrt{2(1-\chi)}\right)\mathrm{d}\chi. \tag{A.15}$$

Appendix A.2. Calculation of P-S scattering cross-sections

In this case we have $\alpha = \text{P}$ and $\beta = \text{S}$, and the polarizations are $\mathbf{p}_{\text{P}}(\mathbf{k}) = \hat{\mathbf{k}}$ and $\mathbf{p}_{\text{S}}(\mathbf{q}) = [\hat{\mathbf{z}}_1(\mathbf{q}), \hat{\mathbf{z}}_2(\mathbf{q})]$. Then $(\hat{\mathbf{k}}\cdot\mathbf{p}_{\text{P}}(\mathbf{k}))^* = 1$, $(\hat{\mathbf{q}}\cdot\mathbf{p}_{\text{S}}(\mathbf{q})) = [0,0]$, $(\hat{\mathbf{q}}\cdot\mathbf{p}_{\text{P}}(\mathbf{k}))^*(\hat{\mathbf{k}}\cdot\mathbf{p}_{\text{S}}(\mathbf{q})) + (\hat{\mathbf{k}}\cdot\hat{\mathbf{q}})(\mathbf{p}_{\text{P}}^*(\mathbf{k})\cdot\mathbf{p}_{\text{S}}(\mathbf{q})) = 2(\hat{\mathbf{k}}\cdot\hat{\mathbf{q}})[\hat{\mathbf{k}}\cdot\hat{\mathbf{z}}_1(\mathbf{q}), \hat{\mathbf{k}}\cdot\hat{\mathbf{z}}_2(\mathbf{q})]$ and $\mathbf{p}_{\text{P}}^*(\mathbf{k})\mathrm{diag}(k_1q_1, k_2q_2, k_3q_3)\mathbf{p}_{\text{S}}(\mathbf{q}) = (\hat{\mathbf{k}}\cdot\hat{\mathbf{q}})[\hat{\mathbf{k}}\cdot\hat{\mathbf{z}}_1(\mathbf{q}), \hat{\mathbf{k}}\cdot\hat{\mathbf{z}}_2(\mathbf{q})]$. From Eq. (A.4), the 1×2 matrix $\mathbf{H}_{\text{PS}}(\mathbf{k},\mathbf{p},\mathbf{q})$ writes:

$$\mathbf{H}_{\text{PS}}(\mathbf{k},\mathbf{p},\mathbf{q}) = \frac{\mathrm{kq}}{\rho}\left[2(\hat{\mathbf{k}}\cdot\hat{\mathbf{q}})[\hat{\mathbf{k}}\cdot\hat{z}_1(\mathbf{q}), \hat{\mathbf{k}}\cdot\hat{z}_2(\mathbf{q})]\widehat{\mu}(\mathbf{p}) + (\hat{\mathbf{k}}\cdot\hat{\mathbf{q}})[\hat{\mathbf{k}}\cdot\hat{z}_1(\mathbf{q}), \hat{\mathbf{k}}\cdot\hat{z}_2(\mathbf{q})]\widehat{\mathcal{A}}(\mathbf{p})\right] \\ = \frac{\mathrm{kq}}{\rho}(\hat{\mathbf{k}}\cdot\hat{\mathbf{q}})[\hat{\mathbf{k}}\cdot\hat{z}_1(\mathbf{q}), \hat{\mathbf{k}}\cdot\hat{z}_2(\mathbf{q})]\left(2\widehat{\mu}(\mathbf{p}) + \widehat{\mathcal{A}}(\mathbf{p})\right), \tag{A.16}$$

and likewise the 2×1 matrix $\mathbf{H}_{\text{SP}}(\mathbf{q},\mathbf{p},\mathbf{k})$ writes:

$$\mathbf{H}_{\text{SP}}(\mathbf{q},\mathbf{p},\mathbf{k}) = \frac{\mathrm{kq}}{\rho}\left[2(\hat{\mathbf{k}}\cdot\hat{\mathbf{q}})[\hat{\mathbf{k}}\cdot\hat{z}_1(\mathbf{q}), \hat{\mathbf{k}}\cdot\hat{z}_2(\mathbf{q})]^T\widehat{\mu}(\mathbf{p}) + (\hat{\mathbf{k}}\cdot\hat{\mathbf{q}})[\hat{\mathbf{k}}\cdot\hat{z}_1(\mathbf{q}), \hat{\mathbf{k}}\cdot\hat{z}_2(\mathbf{q})]^T\widehat{\mathcal{A}}(\mathbf{p})\right] \\ = \frac{\mathrm{kq}}{\rho}(\hat{\mathbf{k}}\cdot\hat{\mathbf{q}})[\hat{\mathbf{k}}\cdot\hat{z}_1(\mathbf{q}), \hat{\mathbf{k}}\cdot\hat{z}_2(\mathbf{q})]^T\left(2\widehat{\mu}(\mathbf{p}) + \widehat{\mathcal{A}}(\mathbf{p})\right). \tag{A.17}$$

Eq. (A.2) writes:

$$\delta(\mathbf{0})(2\pi)^3\sigma_{\text{PS}}^{\text{cubic}}(\mathbf{k},\mathbf{q})[\mathbf{A}_{\text{S}}(\mathbf{q})] = \frac{\pi}{2v_{\text{P}}v_{\text{S}}\mathrm{kq}}\mathbb{E}\left[\mathbf{H}_{\text{PS}}(\mathbf{k},\mathbf{k}-\mathbf{q},\mathbf{q})\mathbf{A}_{\text{S}}(\mathbf{q})\mathbf{H}_{\text{SP}}(\mathbf{q},\mathbf{q}-\mathbf{k},\mathbf{k})\right]\delta\left(\mathrm{k}v_{\text{P}} - \mathrm{q}v_{\text{S}}\right). \tag{A.18}$$

so that inserting Eq. (A.16) and (A.17) yields:

$$\delta(\mathbf{0})(2\pi)^3\sigma_{\text{PS}}^{\text{cubic}}(\mathbf{k},\mathbf{q})[a_{\text{S}}(\mathbf{q})] = \frac{\pi}{2v_{\text{P}}v_{\text{S}}^2\mathrm{kq}}\frac{(\mathrm{kq})^2}{\rho^2}(\hat{\mathbf{k}}\cdot\hat{\mathbf{q}})^2\mathbb{E}\left\{\left[\left(2\widehat{\mu}(\mathbf{k}-\mathbf{q}) + \widehat{\mathcal{A}}(\mathbf{k}-\mathbf{q})\right)\right]\left[\left(2\widehat{\mu}(\mathbf{q}-\mathbf{k}) + \widehat{\mathcal{A}}(\mathbf{q}-\mathbf{k})\right)\right]\right\}\times \\ \times[\hat{\mathbf{k}}\cdot\hat{z}_1(\mathbf{q}), \hat{\mathbf{k}}\cdot\hat{z}_2(\mathbf{q})]a_{\text{S}}(\mathbf{q})[\hat{\mathbf{k}}\cdot\hat{z}_1(\mathbf{q}), \hat{\mathbf{k}}\cdot\hat{z}_2(\mathbf{q})]^T\delta\left(\mathrm{k}K - \mathrm{q}\right). \tag{A.19}$$

Using Eq. (A.10) we get the following P-S differential scattering cross-section operator:

$$\sigma_{\text{PS}}^{\text{cubic}}(\mathbf{k},\mathbf{q})[a_{\text{S}}(\mathbf{q})] = \frac{\pi\mathrm{k}^2\ell_c^3}{2\rho^2 v_{\text{S}}^3}(\hat{\mathbf{k}}\cdot\hat{\mathbf{q}})^2\left(4\nu_\mu^2\Phi_{\mu\mu} + 4\nu_{\mu\mathcal{A}}\Phi_{\mu\mathcal{A}} + \nu_{\mathcal{A}}^2\Phi_{\mathcal{A}\mathcal{A}}\right)(\mathbf{M}(\mathbf{k},\mathbf{q}) : a_{\text{S}}(\mathbf{q}))\,\delta\left(\mathrm{k}K - \mathrm{q}\right) \tag{A.20}$$

in which : denotes the double-dot product and the 2×2 matrix $\mathbf{M}$ is defined as $\mathbf{M}_{ij}(\mathbf{k},\mathbf{q}) = (\hat{\mathbf{k}}\cdot\hat{\mathbf{z}}_i(\mathbf{q}))(\hat{\mathbf{k}}\cdot\hat{\mathbf{z}}_j(\mathbf{q}))$. Note that we have $\mathrm{k}v_{\text{P}} = \mathrm{q}v_{\text{S}}$ (or $\mathrm{q} = \mathrm{k}K$) and thus the argument of the PSDFs is $|\mathbf{k}-\mathbf{q}| = \mathrm{k}\sqrt{1+K^2-2K\chi}$ in which k is

the wavenumber of the P wave mode and $K = v_{\mathrm{P}}/v_{\mathrm{S}} = \sqrt{\kappa_0/\mu_0 + 4/3}$ is the wave speed ratio. Thus, applying the P-S differential scattering cross-section operator to the identity matrix $\mathbf{I}_2$ gives:

$$\sigma_{\mathrm{PS}}^{\mathrm{cubic}}(\mathbf{k},\mathbf{q})[\mathbf{I}_2] = \frac{\pi \mathrm{k}^2 \ell_c^3}{2\rho^2 v_{\mathrm{S}}^3}(\hat{\mathbf{k}}\cdot\hat{\mathbf{q}})^2\left(1-(\hat{\mathbf{k}}\cdot\hat{\mathbf{q}})^2\right)\left(4\nu_\mu^2\Phi_{\mu\mu}+4\nu_{\mu\mathcal{A}}\Phi_{\mu\mathcal{A}}+\nu_{\mathcal{A}}^2\Phi_{\mathcal{A}\mathcal{A}}\right)\delta\left(\mathrm{k}K-\mathrm{q}\right), \tag{A.21}$$

which can be written as a function only of k and χ:

$$\sigma_{\mathrm{PS}}^{\mathrm{cubic}}(\mathrm{k},\chi)[\mathbf{I}_2] = \frac{\pi \mathrm{k}^2 \ell_c^3}{2\rho^2 v_{\mathrm{S}}^3}\chi^2\left(1-\chi^2\right)\left(4\nu_\mu^2\Phi_{\mu\mu}+4\nu_{\mu\mathcal{A}}\Phi_{\mu\mathcal{A}}+\nu_{\mathcal{A}}^2\Phi_{\mathcal{A}\mathcal{A}}\right). \tag{A.22}$$

Setting $\mathcal{A} = 0$ yields the P-S differential scattering cross-section for materials with isotropic fluctuations [2, 6, 37, 26]:

$$\sigma_{\mathrm{PS}}^{\mathrm{iso}}(\mathrm{k},\chi)[\mathbf{I}_2] = \frac{4\pi\nu_\mu^2 \mathrm{k}^2 \ell_c^3}{2\rho^2 v_{\mathrm{S}}^3}\chi^2\left(1-\chi^2\right)\Phi_{\mu\mu}\left(\mathrm{k}\sqrt{1+K^2-2K\chi}\right). \tag{A.23}$$

Following Eq. (A.5) and the hypothesis of equal PSDF, the integration of (A.22) over the wavevector $\mathbf{k}$ gives the P-S total scattering cross-section:

$$\Sigma_{\mathrm{PS}}^{\mathrm{cubic}}(\mathrm{k}) = \frac{\mathrm{k}^4 \ell_c^3}{8\pi\rho^2 v_{\mathrm{P}}^3}\left(4\nu_\mu^2+4\nu_{\mu\mathcal{A}}+\nu_{\mathcal{A}}^2\right)\int_{-1}^{+1}\chi^2\left(1-\chi^2\right)\Phi\left(\mathrm{k}\sqrt{1+K^2-2K\chi}\right)\mathrm{d}\chi, \tag{A.24}$$

for which the classical isotropic S-to-P total scattering cross-section can be retrieved by setting $\mathcal{A}$:

$$\Sigma_{\mathrm{PS}}^{\mathrm{iso}}(\mathrm{k}) = \frac{\nu_\mu^2 \mathrm{k}^4 \ell_c^3}{2\pi\rho^2 v_{\mathrm{P}}^3}\int_{-1}^{+1}\chi^2\left(1-\chi^2\right)\Phi_{\mu\mu}\left(\mathrm{k}\sqrt{1+K^2-2K\chi}\right)\mathrm{d}\chi. \tag{A.25}$$

Appendix A.3. Calculation of S-P scattering cross-sections

Using the same arguments as above, the S-P differential scattering cross-section for cubic anisotropy reads:

$$\sigma_{\mathrm{SP}}^{\mathrm{cubic}}(\mathbf{k},\mathbf{q})[a_{\mathrm{P}}(\mathbf{q})] = \frac{\pi \mathrm{k}^2 \ell_c^3}{2\rho^2 K^3 v_{\mathrm{S}}^3}(\hat{\mathbf{k}}\cdot\hat{\mathbf{q}})^2\left(4\nu_\mu^2\Phi_{\mu\mu}+4\nu_{\mu\mathcal{A}}\Phi_{\mu\mathcal{A}}+\nu_{\mathcal{A}}^2\Phi_{\mathcal{A}\mathcal{A}}\right)\mathbf{M}(\mathbf{q},\mathbf{k})a_{\mathrm{P}}(\mathbf{q})\delta\left(\mathrm{k}-\mathrm{q}K\right), \tag{A.26}$$

so that its application on the identity matrix (unity) gives:

$$\sigma_{\mathrm{SP}}^{\mathrm{cubic}}(\mathbf{k},\mathbf{q})[\mathbf{I}_1] = \frac{\pi \mathrm{k}^2 \ell_c^3}{2\rho^2 K^3 v_{\mathrm{S}}^3}(\hat{\mathbf{k}}\cdot\hat{\mathbf{q}})^2\mathbf{M}(\mathbf{q},\mathbf{k})\left(4\nu_\mu^2\Phi_{\mu\mu}+4\nu_{\mu\mathcal{A}}\Phi_{\mu\mathcal{A}}+\nu_{\mathcal{A}}^2\Phi_{\mathcal{A}\mathcal{A}}\right)\delta\left(\mathrm{k}-\mathrm{q}K\right), \tag{A.27}$$

which in terms of k and χ and ϕ writes:

$$\sigma_{\mathrm{SP}}^{\mathrm{cubic}}(\mathrm{k},\chi,\phi)[\mathbf{I}_1] = \frac{\pi \mathrm{k}^2 \ell_c^3}{2\rho^2 K^3 v_{\mathrm{S}}^3}\left(4\nu_\mu^2\Phi_{\mu\mu}+4\nu_{\mu\mathcal{A}}\Phi_{\mu\mathcal{A}}+\nu_{\mathcal{A}}^2\Phi_{\mathcal{A}\mathcal{A}}\right)\chi^2(1-\chi^2)\begin{bmatrix}\cos^2\phi & \sin\phi\cos\phi\\ \sin\phi\cos\phi & \sin^2\phi\end{bmatrix}. \tag{A.28}$$

A comparison between Eqs. (A.21) and (A.28) yields the following relation between P-S and S-P scattering cross-sections:

$$\mathrm{Tr}\left(\sigma_{\mathrm{SP}}^{\mathrm{cubic}}(\mathrm{k}K,\chi,\phi)[\mathbf{I}_1]\right) = \sigma_{\mathrm{PS}}^{\mathrm{cubic}}(\mathrm{k},\chi)[\mathbf{I}_2]. \tag{A.29}$$

Integrating Eq. (A.28) with respect to the wave vector (knowing that in spherical coordinates the angle ϕ varies in $[0,\pi]$), the diagonal components of the S-P total scattering cross-sections will be equal and the extra-diagonal ones are zero. From Eq. (A.29) one can derive the following relation between P-S and S-P total scattering cross-sections:

$$\mathrm{Tr}\left(\Sigma_{\mathrm{SP}}(\mathrm{k}K)\right) = \frac{1}{2K^3}\Sigma_{\mathrm{PS}}(\mathrm{k}). \tag{A.30}$$

Appendix A.4. Calculation of S-S scattering cross-sections

The objective of this section is to calculate the quadratic S-S scattering cross-section operator $\sigma_{ss}(\mathbf{k},\mathbf{q})$. In this case α = S and β = S. We have $(\hat{\mathbf{k}}\cdot\mathbf{p}_s(\mathbf{k}))^* = [0,0]^T$, $(\hat{\mathbf{q}}\cdot\mathbf{p}_s(\mathbf{q})) = [0,0]$, $(\hat{\mathbf{q}}\cdot\mathbf{p}_s(\mathbf{k}))^*(\hat{\mathbf{k}}\cdot\mathbf{p}_s(\mathbf{q})) + (\hat{\mathbf{k}}\cdot\hat{\mathbf{q}})(\mathbf{p}_s^*(\mathbf{k})\cdot\mathbf{p}_s(\mathbf{q})) = [\hat{\mathbf{q}}\cdot\hat{\mathbf{z}}_1(\mathbf{k}),\hat{\mathbf{q}}\cdot\hat{\mathbf{z}}_2(\mathbf{k})]^T[\hat{\mathbf{k}}\cdot\hat{\mathbf{z}}_1(\mathbf{q}),\hat{\mathbf{k}}\cdot\hat{\mathbf{z}}_2(\mathbf{q})] + (\hat{\mathbf{k}}\cdot\hat{\mathbf{q}})[\hat{\mathbf{z}}_1(\mathbf{k}),\hat{\mathbf{z}}_2(\mathbf{k})]^T[\hat{\mathbf{z}}_1(\mathbf{q}),\hat{\mathbf{z}}_2(\mathbf{q})] = \mathbf{G}(\mathbf{k},\mathbf{q}) + (\hat{\mathbf{k}}\cdot\hat{\mathbf{q}})\mathbf{T}(\mathbf{k},\mathbf{q})$ and $\mathbf{p}_s^*(\mathbf{k})\mathrm{diag}(k_1q_1,k_2q_2,k_3q_3)\mathbf{p}_s(\mathbf{q}) = 0\times\mathbf{I}_2$. In these equations the 2×2 matrices $\mathbf{G}$ and $\mathbf{T}$ are respectively defined as $\mathbf{G}_{ij}(\mathbf{k},\mathbf{q}) = (\hat{\mathbf{q}}\cdot\hat{\mathbf{z}}_i(\mathbf{k}))(\hat{\mathbf{k}}\cdot\hat{\mathbf{z}}_j(\mathbf{q}))$ and $\mathbf{T}_{ij}(\mathbf{k},\mathbf{q}) = (\hat{\mathbf{z}}_i(\mathbf{k})\cdot\hat{\mathbf{z}}_j(\mathbf{q}))$. It should be pointed out that since in this case the first and the last terms in the right hand side of the Eq. (A.4) are both zero, the influence of the anisotropy parameter vanishes so that the S-S scattering parameters will become identical between cubic and isotropic cases.

Inserting these equations into (A.4) yields:

$$\mathbf{H}_{ss}(\mathbf{k},\mathbf{p},\mathbf{q}) = \frac{\mathrm{kq}}{\rho}\left[\mathbf{G}(\mathbf{k},\mathbf{q}) + (\hat{\mathbf{k}}\cdot\hat{\mathbf{q}})\mathbf{T}(\mathbf{k},\mathbf{q})\right]\widehat{\mu}(\mathbf{p}). \tag{A.31}$$

From Eq. (A.2) we have:

$$\delta(\mathbf{0})(2\pi)^3\sigma_{ss}(\mathbf{k},\mathbf{q})[a_s(\mathbf{q})] = \frac{\pi}{2v_s^2\mathrm{kq}}\mathbb{E}\left[\mathbf{H}_{ss}(\mathbf{k},\mathbf{k}-\mathbf{q},\mathbf{q})a_s(\mathbf{q})\mathbf{H}_{ss}(\mathbf{q},\mathbf{q}-\mathbf{k},\mathbf{k})\right]\delta\left(v_s(\mathrm{k}-\mathrm{q})\right). \tag{A.32}$$

Introducing (A.31) into this equation yields:

$$\delta(\mathbf{0})(2\pi)^3\sigma_{ss}(\mathbf{k},\mathbf{q})[a_s(\mathbf{q})] = \frac{\pi\mathrm{kq}}{2\rho^2v_s^2}\mathbb{E}\left\{\left[\mathbf{G}(\mathbf{k},\mathbf{q}) + (\hat{\mathbf{k}}\cdot\hat{\mathbf{q}})\mathbf{T}(\mathbf{k},\mathbf{q})\right]\widehat{\mu}(\mathbf{k}-\mathbf{q})a_s(\mathbf{q})\right.$$
$$\left.\left[\mathbf{G}(\mathbf{q},\mathbf{k}) + (\hat{\mathbf{k}}\cdot\hat{\mathbf{q}})\mathbf{T}(\mathbf{q},\mathbf{k})\right]\widehat{\mu}(\mathbf{q}-\mathbf{k})\right\}\delta\left(v_s(\mathrm{k}-\mathrm{q})\right), \tag{A.33}$$

or

$$\sigma_{ss}^{\mathrm{cubic}}(\mathbf{k},\mathbf{q})[a_s(\mathbf{q})] = \frac{\pi\mathrm{k}^2\ell_c^3}{2\rho^2v_s^3}v_\mu^2\Phi_{\mu\mu}\left[\mathbf{G}(\mathbf{k},\mathbf{q})a_s(\mathbf{q})\mathbf{G}(\mathbf{q},\mathbf{k}) + (\hat{\mathbf{k}}\cdot\hat{\mathbf{q}})\left[\mathbf{G}(\mathbf{k},\mathbf{q})a_s(\mathbf{q})\mathbf{T}(\mathbf{q},\mathbf{k}) + \mathbf{T}(\mathbf{k},\mathbf{q})a_s(\mathbf{q})\mathbf{G}(\mathbf{q},\mathbf{k})\right]\right.$$
$$\left.+(\hat{\mathbf{k}}\cdot\hat{\mathbf{q}})^2\mathbf{T}(\mathbf{k},\mathbf{q})a_s(\mathbf{q})\mathbf{T}(\mathbf{q},\mathbf{k})\right]\delta(\mathrm{k}-\mathrm{q}), \tag{A.34}$$

in which the argument of all the PSDFs is $|\mathbf{k}-\mathbf{q}| = \mathrm{k}\sqrt{2(1-\chi)}$, as for the case of P-P scattering but this time with $\mathrm{k} = \omega/v_s$ the wavenumber of the S mode. Applying the S-S scattering cross-section opertator to the identity matrix $\mathbf{I}_2$ gives the following representation in terms of the wavenumber k and χ as:

$$\sigma_{ss}^{\mathrm{cubic}}(\mathrm{k},\chi)[\mathbf{I}_2] = \sigma_{ss}^{\mathrm{iso}}(\mathrm{k},\chi)[\mathbf{I}_2] = \frac{\pi v_\mu^2\mathrm{k}^2\ell_c^3}{2\rho^2v_s^3}\left(4\chi^4-3\chi^2+1\right)\Phi_{\mu\mu}\left(\mathrm{k}\sqrt{2(1-\chi)}\right)\mathbf{I}_2. \tag{A.35}$$

Following Eq. (A.5) and the hypothesis on the PSDF, the integration of (A.35) over the wavevector $\mathbf{k}$ yields the S-S total scattering cross-section for a heterogeneous material with isotropic background and cubic fluctuations:

$$\Sigma_{ss}^{\mathrm{cubic}}(\mathrm{k}) = \Sigma_{ss}^{\mathrm{iso}}(\mathrm{k}) = \frac{v_\mu^2\mathrm{k}^4\ell_c^3}{16\pi\rho^2v_s^3}\mathbf{I}_2\int_{-1}^{+1}\left(4\chi^4-3\chi^2+1\right)\Phi\left(\mathrm{k}\sqrt{2(1-\chi)}\right)\mathrm{d}\chi, \tag{A.36}$$

References

[1] S. Chandrasekhar, Radiative transfer, Dover Publications, 1960.

[2] R. L. Weaver, Diffusivity of ultrasound in polycrystals, Journal of the Mechanics and Physics of Solids 38 (1990) 55–86.

[3] Y. Zeng, Theory of scattered P-wave and S-wave energy in a random isotropic scattering medium, Bulletin of the Seismological Society of America 83 (1993) 1264–1276.

[4] H. Sato, Multiple isotropic scattering model including P-S conversions for the seismogram envelope formation, Geophysical Journal International 117 (1994) 487–494.

[5] J. A. Turner, R. L. Weaver, Radiative transfer and multiple scattering of diffuse ultrasound in polycrystalline media, Journal of the Acoustical Society of America 96 (1994) 3675–3683.

[6] L. Ryzhik, G. Papanicolaou, J. B. Keller, Transport equations for elastic and other waves in random media, Wave Motion 24 (1996) 327–370.

[7] L. Margerin, M. Campillo, B. A. van Tiggelen, Monte carlo simulation of multiple scattering of elastic waves, Journal of Geophysical Research 105 (2000) 7873–7892.
[8] J. A. Turner, Elastic wave propagation and scattering in heterogeneous, anisotropic media: Textured polycrystalline materials, Journal of the Acoustical Society of America 106 (1999) 541–552.
[9] J. Przybilla, M. Korn, Monte Carlo simulation of radiative energy transfer in continuous elastic random media – three-component envelopes and numerical validation, Geophysical Journal International 173 (2008) 566–576.
[10] P. J. Gaebler, T. Eulenfeld, U. Wegler, Seismic scattering and absorption parameters in the W-Bohemia/Vogtland region from elastic and acoustic radiative transfer theory, Geophysical Journal International 201 (2015) 1471–1481.
[11] C. J. Sanborn, V. F. Cormier, M. Fitzpatrick, Combined effects of deterministic and statistical structure on high-frequency regional seismograms, Geophysical Journal International 210 (2017) 1143–1159.
[12] N. M. Shapiro, M. Campillo, L. Margerin, S. K. Singh, V. Kostoglodov, J. Pacheco, The energy partitioning and the diffusive character of the seismic coda, Bulletin of the Seismological Society of America 90 (2000) 655–665.
[13] R. Hennino, N. Trégourès, N. M. Shapiro, L. Margerin, M. Campillo, B. A. V. Tiggelen, Weaver, Observation of equipartition of seismic waves, Physical Review Letters 86 (2001) 3447.
[14] R. Weaver, O. Lobkis, Ultrasonics without a source: Thermal fluctuation correlations at mhz frequencies, Physical Review Letters 87 (2001) 134301.
[15] M. Campillo, A. Paul, Long-range correlations in the diffuse seismic coda, Science 299 (2003) 547–549.
[16] T. Saito, H. Sato, M. Fehler, M. Ohtake, Simulating the envelope of scalar waves in 2d random media having power-law spectra of velocity fluctuation, Bulletin of the Seismological Society of America 93 (2003) 240–252.
[17] L. Borcea, G. Papanicolaou, C. Tsogka, Coherent interferometric imaging in clutter, Geophysics 71 (2006) SI165–SI175.
[18] H. Kawase, F. J. Sánchez-Sesma, S. Matsushima, The optimal use of horizontal-to-vertical spectral ratios of earthquake motions for velocity inversions based on diffuse-field theory for plane waves, Bulletin of the Seismological Society of America 101 (2011) 2001–2014.
[19] F. J. Sánchez-Sesma, R. L. Weaver, H. Kawase, S. Matsushima, F. Luzón, M. Campillo, Energy partitions among elastic waves for dynamic surface loads in a semi-infinite solid, Bulletin of the Seismological Society of America 101 (2011) 1704–1709.
[20] H. Sato, M. Fehler, T. Maeda, Seismic Wave Propagation and Scattering in the Heterogeneous Earth: Second Edition, SpringerLink : Bücher, Springer Berlin Heidelberg, 2012.
[21] O. A. Grigorev, T. D. Shemergor, Propagation of ultrasonic waves in polycrystals of cubic symmetry with allowance for multiple scattering, Journal of Applied Mathematics and Mechanics 44 (1980) 217–223.
[22] S. Hirsekorn, The scattering of ultrasonic waves by polycrystals, Journal of the Acoustical Society of America 72 (1982) 1021–1031.
[23] F. E. Stanke, G. S. Kino, A unified theory for elastic wave propagation in polycrystalline materials, Journal of the Acoustical Society of America 75 (1984) 665–681.
[24] C. B. Guo, P. Höller, K. Goebbels, Scattering of ultrasonic waves in anisotropic polycrystalline metals, Acustica 59 (1985) 112–120.
[25] O. Engler, V. Randle, Introduction to texture analysis: macrotexture, microtexture and orientation mapping, CRC Press, 2009.
[26] I. Baydoun, E. Savin, R. Cottereau, D. Clouteau, J. Guilleminot, Kinetic modeling of multiple scattering of elastic waves in heterogeneous anisotropic media, Wave Motion 51 (2014) 1325–1348.
[27] Q. Ta, D. Clouteau, R. Cottereau, Modeling of random anisotropic elastic media and impact on wave propagation, European Journal of Computational Mechanics 19 (2010) 241–253.
[28] K. Shiomi, H. Sato, M. Ohtake, Broad-band power-law spectra of well-log data in Japan, Geophysical Journal International 130 (1997) 57–64.
[29] W. Voigt, Lehrbuch der kristallphysik, Teubner, Berlin (1928).
[30] P. Chadwick, M. Vianello, S. C. Cowin, A new proof that the number of linear elastic symmetries is eight, Journal of the Mechanics and Physics of Solids 49 (2001) 2471–2492.
[31] J. Guilleminot, C. Soize, On the statistical dependence for the components of random elasticity tensors exhibiting material symmetry properties, Journal of Elasticity 111 (2013) 109–130.
[32] L. Klimeš, Correlation functions of random media, Pure and Applied Geophysics 159 (2002) 1811–1831.
[33] S. Khazaie, R. Cottereau, D. Clouteau, Influence of the spatial correlation structure of an elastic random medium on its scattering properties, Journal of Sound and Vibration 370 (2016) 132 – 148.
[34] G. Bal, O. Pinaud, Accuracy of transport models for waves in random media, Wave Motion 43 (2006) 561–578.
[35] R. L. Weaver, On diffuse waves in solid media, Journal of the Acoustical Society of America 71 (1982) 1608–1609.
[36] G. Papanicolaou, L. Ryzhik, J. B. Keller, Stability of the P to S energy ratio in the diffusive regime, Bulletin of the Seismological Society of America 86 (1996) 1107–1115.
[37] J. A. Turner, Scattering and diffusion of seismic waves, Bulletin of the Seismological Society of America 88 (1998) 276–283.
[38] L. Margerin, Diffusion approximation with polarization and resonance effects for the modelling of seismic waves in strongly scattering small-scale media, Geophysical Journal International 192 (2013) 326–345.
[39] N. P. Trégourès, B. A. van Tiggelen, Generalized diffusion equation for multiple scattered elastic waves, Waves in Random Media 12 (2002) 21–38.
[40] L. Margerin, B. A. van Tiggelen, M. Campillo, Effect of absorption on energy partition of elastic waves in the seismic coda, Bulletin of the Seismological Society of America 91 (2001) 624–627.
[41] H. Nakahara, K. Yoshimoto, Radiative transfer of elastic waves in two-dimensional isotropic scattering media: Semi-analytical approach for isotropic source radiation, Earth, Planets and Space 63 (2011) 459–468.
[42] P. Cupillard, E. Delavaud, G. Burgos, G. Festa, J.-P. Vilotte, Y. Capdeville, J.-P. Montagner, RegSEM: a versatile code based on the spectral element method to compute seismic wave propagation at the regional scale, Geophysical Journal International 188 (2012) 1203–1220.
[43] R. Cottereau, D. Clouteau, J.-P. Vilotte, R. Madariaga, Validation of software for 3D propagation of waves in heterogeneous and random media, 9th US National Congress on Computational Mechanics (USNCCM) (2007).
[44] S. Khazaie, R. Cottereau, D. Clouteau, Numerical observation of the equipartition regime in a 3D random elastic medium, and discussion of

the limiting parameters, Computers & Geosciences 102 (2017) 56–67.
[45] A. Panunzio, R. Cottereau, G. Puel, Large scale random fields generation using localized Karhunen-Loève expansion, Advanced Modeling and Simulation in Engineering Sciences 5 (2018) 1–21.
[46] M. Shinozuka, G. Deodatis, Simulation of stochastic processes by spectral representation, Applied Mechanics Reviews 44 (1991) 191–204.
[47] L. de Carvalho Paludo, V. Bouvier, R. Cottereau, Scalable parallel scheme for sampling of Gaussian random fields over large domains, International Journal for Numerical Methods in Engineering 117 (2019) 845–859.
[48] G. Bal, T. Komorowski, L. Ryzhik, Self-averaging of wigner transforms in random media, Communications in Mathematical Physics 242 (2003) 81–135.
[49] K. F. Graff, Wave motion in elastic solids, Courier Corporation, 2012.
[50] K. Aki, P. G. Richards, Quantitative seismology, 2002.
[51] L. Margerin, Attenuation, transport and diffusion of scalar waves in textured random media, Tectonophysics 416 (2006) 229 – 244.